



Professor Néstor Armesto during one of the lectures of his course (in collaboration with Professor Carlos Pajares) Quantum Chromodynamics at the Third IDPASC School (picture by C. Merino)

# Quantum Chromodynamics

Néstor Armesto and Carlos Pajares

**Abstract** In this chapter we present some selected topics in the quantum field theory of the strong interaction, Quantum Chromodynamics. After an introduction on the gauge symmetry in Sect. 1, we briefly present the Renormalisation Group Equation in Sect. 2. Afterwards we turn to asymptotic freedom in Sect. 3 and confinement in Sect. 4. Then, after briefly reviewing the QCD colour factors in Sect. 5, we describe the symmetries of the theory in Sect. 6: isospin, chiral and scale symmetries, and the vacuum structure is reviewed with an introduction about instantons. In Sect. 7 the phase diagram is presented. Finally, in Sect. 8 some phenomenological applications of perturbative Quantum Chromodynamics are reviewed:  $e^+e^-$  annihilation, deep inelastic scattering, factorisation, radiation and jets.

## 1 Introduction

Quantum Chromodynamics (QCD) is the theory of the strong force describing the interactions of quarks forming hadrons, mesons if the interaction is between a quark and an antiquark and baryons if the interaction is among three quarks.

The interaction of quarks is via the exchange of gluons that carry a new quantum number, the colour. The colour was first introduced by Greenberg in order to restore the Pauli principle. The quarks have spin  $1/2$ , three quarks cannot have the same quantum numbers. The baryons  $\Delta^{++}$ ,  $\Delta^-$  and  $\Omega^-$  are formed by three quarks  $uuu$ ,  $ddd$  and  $sss$  respectively. Therefore, each quark must have an additional quantum number, the colour, arranged in such a way that each quark has one of three possible values, surviving the Pauli principle. Later, the colour was introduced dynamically by Han and Nambu, in a non-abelian gauge theory where the gauge bosons are the gluons. The theory has a similar structure to Quantum Electrodynamics (QED), but

---

N. Armesto (✉) · C. Pajares

Departamento de Física de Partículas and IGFAE, Universidade de Santiago de Compostela,  
15782 Santiago de Compostela, Galicia-Spain  
e-mail: nestor.armesto@usc.es

C. Pajares

e-mail: pajares@fpaxpl.usc.es

© Springer International Publishing Switzerland 2015

C. Merino (ed.), *Lectures on Particle Physics, Astrophysics and Cosmology*,  
Springer Proceedings in Physics 161, DOI 10.1007/978-3-319-12238-0\_2

now the group,  $SU(3)$ , is non abelian and hence the gluons are self-interacting. This fact is very important, implying asymptotic freedom [1, 2] at high energies and strong interactions at low energies. These interactions imply confinement, meaning that only colour-singlet states can propagate at large distances. The colour-singlet stable states are mesons ( $q\bar{q}$ ) and baryons ( $qqq$ ). There are excellent textbooks about QCD where you can find more details [3–9].

There are many similarities between QED and QCD. QED is a gauge theory, whose gauge group is  $U(1)$ , and the structure of the lagrangian is derived from this gauge symmetry. In fact, we start from the lagrangian of non-interacting matter

$$\mathcal{L}_0 = \bar{\psi}(i\not{d} - m)\psi, \quad (1)$$

with  $d = a_\mu \gamma^\mu$  and  $\gamma^\mu$  are the Dirac matrixes satisfying

$$\{\gamma^\mu, \gamma^\nu\} = 2g^{\mu\nu}, \quad (2)$$

with  $g^{\mu\nu}$  the metric tensor. The lagrangian (1) is invariant under the global gauge transformation

$$\begin{aligned} \psi &\longrightarrow \psi' = \exp[iq\alpha]\psi, \\ \bar{\psi} &\longrightarrow \bar{\psi}' = \exp[-iq\alpha]\bar{\psi}. \end{aligned} \quad (3)$$

The QED lagrangian is derived asking how we must modify (1) to make it also invariant under local changes of gauge i.e. when  $\alpha$  in (3) is a function  $\alpha(x)$ . Now, we have

$$\partial_\mu(\exp[iq\alpha(x)]\psi) = \exp[iq\alpha(x)](\partial_\mu\psi(x) + iq\partial_\mu\alpha(x)\psi(x)). \quad (4)$$

There is an extra term which breaks the invariance of the lagrangian (1).

In order to make (1) invariant, one may consider the addition of new terms to compensate the extra term. This can be done by introducing the gauge field  $A_\mu$ , which transforms under the local change of gauge like

$$A_\mu \longrightarrow A'_\mu = A_\mu - \partial_\mu\alpha(x) = A_\mu + \frac{i}{q}\partial_\mu(\exp[iq\alpha(x)])\exp[-iq\alpha(x)] \quad (5)$$

and by replacing the derivative  $\partial_\mu$  by the covariant derivative

$$D_\mu = \partial_\mu + iqA_\mu. \quad (6)$$

As we have introduced the gauge field, we must add to the lagrangian the corresponding kinetic term

$$\mathcal{L}_A = -\frac{1}{4}F_{\mu\nu}F^{\mu\nu}, \quad (7)$$

where the field stress tensor is defined by

$$F_{\mu\nu} = \partial_\mu A_\nu - \partial_\nu A_\mu \quad (8)$$

and the QED lagrangian is therefore given by

$$\mathcal{L}_{QED} = \bar{\psi}(i\not{D} - m)\psi - \frac{1}{4}F_{\mu\nu}F^{\mu\nu} \quad (9)$$

which is now gauge invariant. Note that there is not any term  $\frac{1}{2}m_\gamma^2 A^\mu A_\mu$  corresponding to the mass of the gauge field because it is not gauge invariant. The new lagrangian contains the free lagrangians and the interaction lagrangian:

$$\mathcal{L}_{QED} = \mathcal{L}_0 + \mathcal{L}_A - j^\mu A_\mu, \quad j^\mu = q\bar{\psi}\gamma^\mu\psi. \quad (10)$$

Therefore, the gauge symmetry determines the interaction. This interaction is illustrated in Fig. 1, where an electron ( $\psi$ ) emits a photon ( $A_\mu$ ) and goes along its path.

QCD can be derived in the same way as QED [10]. We start from the lagrangian density for non-interacting quarks:

$$\mathcal{L}_q = \sum_q \bar{\psi}_q^j i\not{D}\psi_q^k - \sum_q m_q \bar{\psi}_q^j \psi_q^j, \quad (11)$$

where the indices  $j, k = 1, 2, 3$  stand for the colour and  $q = d, u, s, c, b, t$  denotes the flavour. The gauge group is  $SU(N_c)$  with  $N_c = 3$ . Each element  $U$  of  $SU(N_c)$  infinitesimally close to the identity can be written as

$$U = I + iG, \quad (12)$$

where  $G$  are hermitian traceless matrixes. One can choose a set of  $N_c^2 - 1$  matrixes such that any  $G$  can be written as

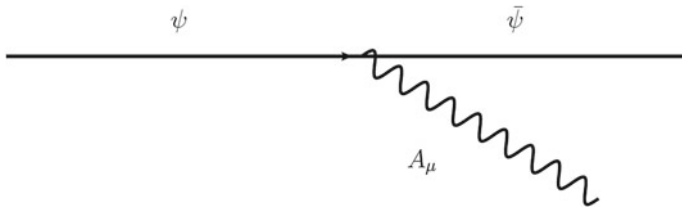


**Fig. 1** Diagram of the interaction in QED

$$G = \sum_{a=1}^{N_c^2-1} \alpha_a t_a, \quad (13)$$

with  $\alpha_a$  some coefficients. It can be shown that  $[t_a, t_b]$  are antihermitian and traceless and, hence, they must be a linear combination of the basis  $t_c$ ,

$$[t_a, t_b] = i f_{abc} t_c, \quad (14)$$

where  $f_{abc}$  are real constant, antisymmetric in all their indices. Equation (14) defines the algebra of the group. The  $(N_c^2 - 1) \times (N_c^2 - 1)$  matrixes  $T_a$  obeying

$$(T_a)_{bc} = -i f_{abc}, \quad (15)$$

$$[T_a, T_b] = i f_{abc} T_c, \quad (16)$$

define the adjoint representation of the group, while the  $t_a$  define the fundamental representation of the group.

Now, the transformation of the gauge fields reads

$$\begin{aligned} \psi_q(x) &\longrightarrow \psi'_q(x) = \exp[i g_s \alpha_a(x) T_a] \psi_q(x), \\ \bar{\psi}_q(x) &\longrightarrow \bar{\psi}'_q(x) = \exp[-i g_s \alpha_a(x) T_a] \bar{\psi}_q(x), \end{aligned} \quad (17)$$

where  $g_s$  is the coupling constant of the strong interaction.

In order to make the lagrangian (11) invariant, we introduce  $N_c^2 - 1$  gauge fields (gluons)  $G_\mu^a$ , transforming as

$$G_\mu^a \longrightarrow G_\mu^{a'} = G_\mu^a - \partial_\mu \alpha_a(x) - g_s f_{abc} \alpha_b(x) G_\mu^c, \quad (18)$$

and replace the derivative  $\partial_\mu$  by the covariant derivative  $D_\mu$ , with

$$D_\mu = \partial_\mu + i g_s T_a G_\mu^a. \quad (19)$$

Now, comparing with the QED (5), we have introduced an additional term required to cancel the additional term appearing when the transformation (17) is introduced in the free lagrangian (11), due to the non-abelian composition law of  $T_a$ .

We have to introduce again a kinetic term for the gauge fields

$$\mathcal{L}_G = -\frac{1}{4} F_a^{\mu\nu} F_{\mu\nu}^a, \quad (20)$$

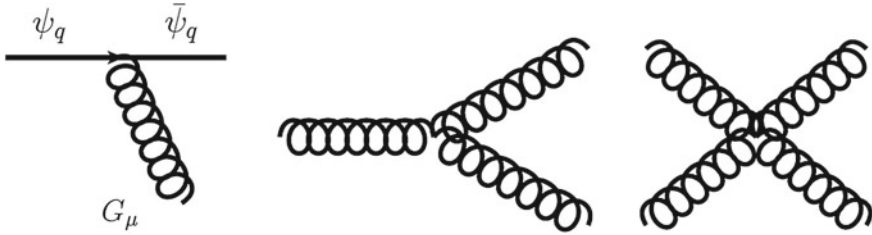


**Fig. 2** Diagram of the interactions in QCD

where

$$F_{\mu\nu}^a = \partial_\mu G_\nu^a - \partial_\nu G_\mu^a - g_s f_{abc} G_\mu^b G_\nu^c. \quad (21)$$

Note that there is an extra term in (21) comparing to QED, because otherwise (20) would not be gauge invariant.

We observe that in addition to the term  $-j_a^\mu G_\mu^a$  with

$$j_a^\mu = g_s \bar{\psi}_q \gamma^\mu \psi_q T_a, \quad (22)$$

corresponding to the emission of the gluon  $T_a G_\mu^a$  by a quark  $\psi_q$  as represented in Fig. 2, similar to the emission of a photon by a charged particle in the case of QED, we have, according to (20) and (21) the emission of a gluon by a gluon, and the coupling of two gluons to two gluons, Fig. 2. These terms have important consequences. They will give rise to asymptotic freedom at high energies and strong interactions at low energies contrary to what happens in QED. From now on we will use for the coupling constant  $\alpha_s = g_s^2/(4\pi)$  instead of  $g_s$ .

## 2 Renormalisation Group Equation

The renormalisation group equation exploits the requirement that a physical quantity  $\Gamma$  does not depend on the particular scale at which it is renormalised. The approach was first introduced by Stückelberg, Peterman, Gell-Mann and Low in the 50s, and later by Callan and Symanzik. Let us denote by  $\Gamma_B(s, \alpha_0, \Lambda^2)$  the bare quantity, where  $\alpha_0$  is the bare coupling and  $\Lambda$  is the ultraviolet cut-off to regularise the unrenormalised quantity. The renormalised quantity  $\Gamma$  is defined at scale  $\mu^2$ , and also the coupling constant  $\alpha(\mu)$  and the normalisation scale factor  $Z$  such that

$$\Gamma(s, \alpha(\mu), \mu^2) = Z(\mu^2) \Gamma_B(s, \alpha_0, \Lambda^2). \quad (23)$$

$\Gamma_B$  has to be independent of the choice of scale  $\mu^2$ , therefore

$$\frac{d\Gamma_B}{d\mu^2} = 0, \quad (24)$$

which can be written as

$$\mu^2 \frac{\partial \Gamma}{\partial \mu^2} + \mu^2 \frac{\partial \alpha}{\partial \mu^2} \frac{\partial \Gamma}{\partial \alpha} - \mu^2 \frac{\Gamma}{Z} \frac{\partial Z}{\partial \mu^2} = 0. \quad (25)$$

Defining

$$\beta(\alpha) = \mu^2 \frac{\partial \alpha}{\partial \mu^2} \quad (26)$$

and

$$\gamma(\alpha) = -\mu^2 \frac{\Gamma}{Z} \frac{\partial Z}{\partial \mu^2}, \quad (27)$$

(25) becomes

$$\left[ \mu^2 \frac{\partial}{\partial \mu^2} + \beta(\alpha) \frac{\partial}{\partial \alpha} + \gamma(\alpha) \right] \Gamma(s, \alpha(\mu), \mu^2) = 0, \quad (28)$$

which is known as the renormalisation group equation that expresses how you must compensate a change in the scale  $\mu^2$ , changing the coupling constant and the overall scale factor  $Z$ .

### 3 Charge Screening: Asymptotic Freedom

From (26), we can write

$$\ln \left( \frac{\mu^2}{\mu_0^2} \right) = \int_{\alpha(\mu_0^2)}^{\alpha(\mu^2)} \frac{d\alpha}{\beta(\alpha)}. \quad (29)$$

In QCD,  $\beta(\alpha)$  can be calculated perturbatively with the result

$$\beta(\alpha_s) = -b_0 \alpha_s^2 - b_1 \alpha_s^3 + \mathcal{O}(\alpha_s^4), \quad (30)$$

with

$$b_0 = \frac{11N_c - 2N_f}{12\pi},$$

$$b_1 = \frac{17N_c^2 - [5N_c + 3(N_c^2 - 1)/(2N_c)]N_f}{24\pi^2}, \quad (31)$$

with  $N_f$  the number of active flavours. Retaining the first term of (30) in (29), we obtain

$$\alpha_s(\mu^2) = \frac{\alpha_s(\mu_0^2)}{1 + \alpha_s(\mu_0^2)b_0 \ln(\mu^2/\mu_0^2)}. \quad (32)$$

We observe that for large  $\mu^2$  or small distances  $r^2 \sim 1/\mu^2$ , we obtain asymptotic freedom,  $\alpha_s(\mu^2) \rightarrow 0$ . This behaviour is opposite to the one in QED, where

$$\alpha_{em}(\mu^2) = \frac{\alpha_{em}(\mu_0^2)}{1 - \frac{\alpha_{em}(\mu_0^2)}{3\pi} \ln(\mu^2/\mu_0^2)}. \quad (33)$$

Here, for  $r^2 < r_0^2$  ( $\mu^2 > \mu_0^2$ ),  $\alpha_{em}(\mu^2) > \alpha_{em}(\mu_0^2)$ , and the effective charge grows at smaller distances. This behaviour is nothing but the charge screening effect in QED. In fact, if we consider the electric field produced by two charges located in a medium, the particles in the medium are oriented in the direction of the electric field, producing a reduction of the effective value of the two charges (Fig. 3). Close to each charge, the effective charge is the original charge (bare) minus the induced charge, therefore at smaller distances the screening is smaller and the value of the effective charge becomes closer to the value of the original charge (Fig. 4).

Microscopically, the bare charge is given by the left diagram in Fig. 5. In addition to this diagram, at lowest order in  $\alpha_{em}$  we have another diagram (Fig. 5 right) giving rise to (33). The  $e^+e^-$  pairs in Fig. 5 (right) lead to charge screening.

In QCD, in addition to similar diagrams to those in QED, we have another diagram, see Fig. 6c, that changes the sign of the denominator of (33) if  $11N_c - 2N_f > 0$ . The evolution of the coupling constant  $\alpha_s$  according to (32) has been checked in deep inelastic scattering,  $e^+e^-$  annihilation and heavy flavour experiments as it is shown in Fig. 7.

Although the lagrangian of massless QCD has no scale, the renormalisation introduces a dimensional scale parameter. In fact, from (29) we have

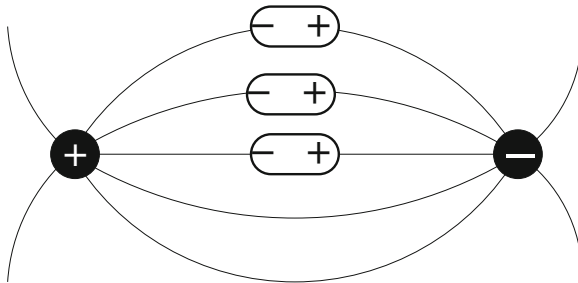


**Fig. 3** Polarisation of a medium in QED



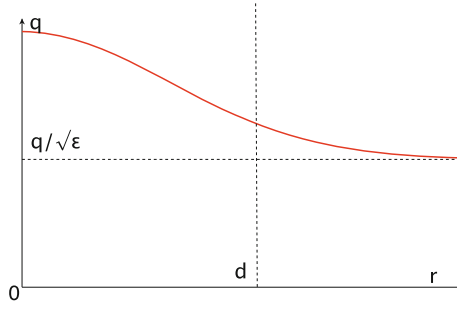


**Fig. 4** Effective charge in a polarisable QED medium

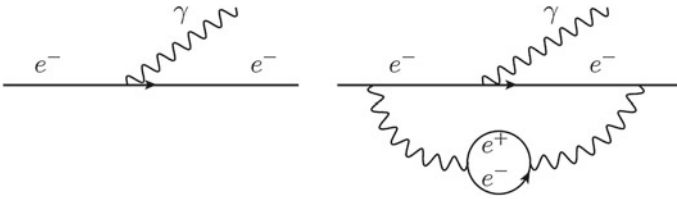


**Fig. 5** Diagrams contributing to charge renormalisation in QED

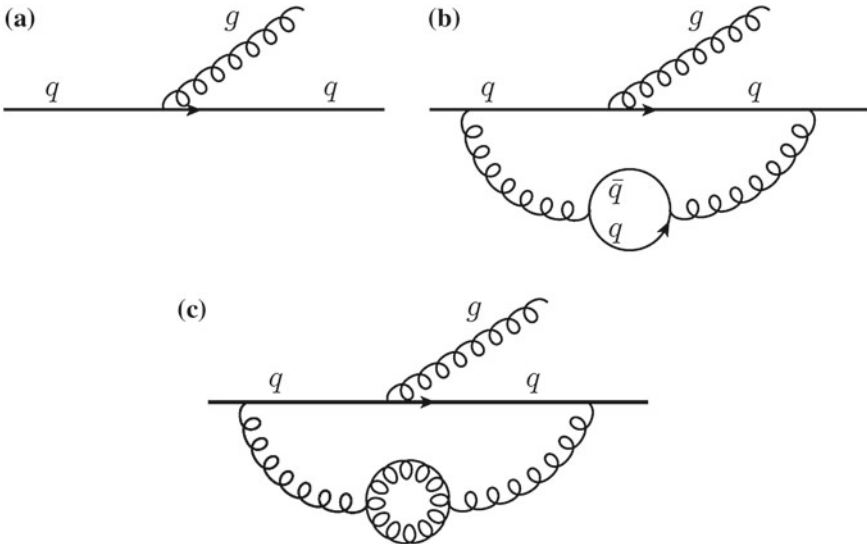


**Fig. 6** Diagrams contributing to charge renormalisation in QCD

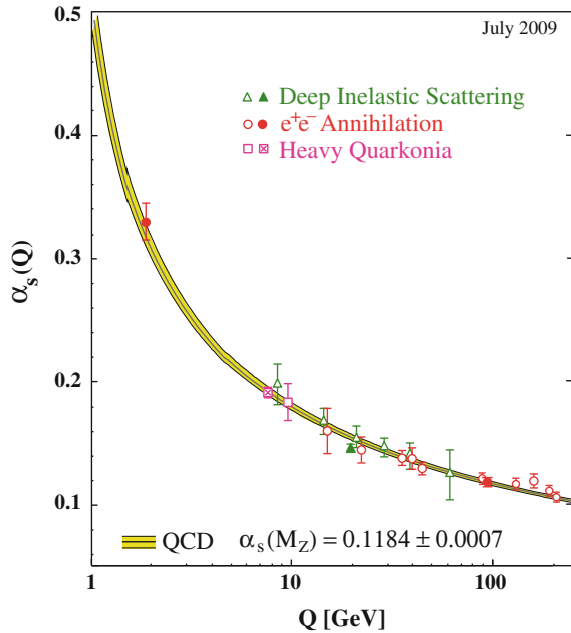


**Fig. 7** Compilation of results on the evolution of the strong coupling constant  $\alpha_s$  with momentum  $Q \propto 1/r$ , taken from [11]

$$\Lambda^2 = \mu^2 \exp \left( - \int^{\alpha_s(\mu^2)} \frac{dx}{\beta(x)} \right). \quad (34)$$

Equation (32) is derived from (34) taking the leading order expression for  $\beta(x)$ . It could be said that  $\Lambda$  is the scale at which the coupling constant becomes infinite. However, this is not self-consistent because we use the first term for  $\beta(x)$  in a region where the coupling is large. More generally, we can say that  $\Lambda$  is the scale where QCD becomes non-perturbative.

## 4 Confinement

In QCD, the particles associated to the fields, quarks and gluons, are not asymptotic free states opposite to most of the field theories. Quarks and gluons are confined inside hadrons. This behaviour in QCD is not understood analytically, see [12, 13], and only doing some approximation it can be obtained. There are lattice numerical simulations that allow to reproduce some of the consequences of confinement, the masses of the different hadrons [14]. Notice that more of 95 % of hadron masses is due to the strong interaction and not to the quark masses that are quite small.

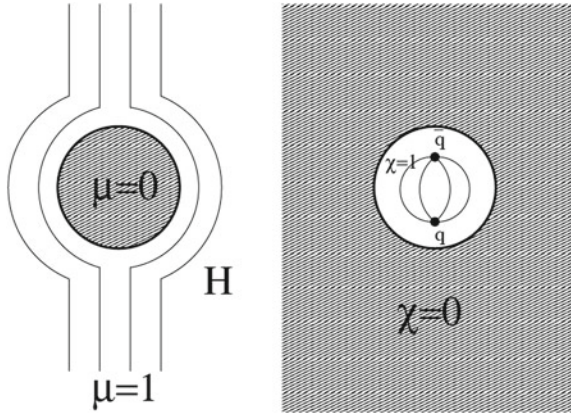


**Fig. 8** Illustration of the picture of the dual superconductor

In analogy with QED, confinement can be seen in the following way: the QCD vacuum can be regarded as a gluon and quark–antiquark condensate, being a perfect dielectric (colour dielectric constant  $\chi = 0$ ) similarly to the electron pairs in a superconductor in QED. In this case, the superconductor is a perfect diamagnet (magnetic susceptibility  $\mu = 0$ ). The role of the magnetic field in QED is played by the chromoelectric field in QCD, the QED superconductor is the QCD vacuum and the QED vacuum ( $\mu = 1$ ) is the inside of the hadron in QCD ( $\chi = 1$ ). The role of the inside and outside in QED and QCD are exchanged. Due to this, this picture is known as the dual superconductor picture. In the same way that the magnetic field is expelled from the superconductor, the chromoelectric field is expelled from the QCD vacuum that pushes it towards the inside of the hadron, implying colour confinement as illustrated in Fig. 8.

## 5 QCD Colour Factors: Jet Structure

In the computation of cross sections, the involved states have to be summed or averaged giving rise to colour factors. In order to compute them, we use the properties of  $SU(3)$  or  $SU(N_c)$ . The relevant properties of the fundamental representation of QCD,  $t^a$  used for quarks, and of the adjoint matrix representation of QCD,  $T^a$  used for gluons, are (14)–(16). The  $t^a$  are normalised such that

$$\text{tr}(t^a t^b) = T_F \delta^{ab} = \frac{1}{2} \delta^{ab}, \quad (35)$$

and the colour matrixes satisfy the following relations:



**Fig. 9** Diagrams of the quark–gluon, gluon–gluon and quark–antiquark loops (from left to right) to which the colour factors  $C_F$ ,  $C_A$  and  $T_F$  are respectively associated

$$\sum_a (t^a)_{ik} (t^a)_{kj} = C_F \delta_{ij}, \quad C_F = \frac{N_c^2 - 1}{2N_c},$$

$$\text{tr}(T^a T^b) = \sum_{c,d} f^{acd} f^{bcd} = C_A \delta^{ab}, \quad C_A = N_c, \quad (36)$$

where  $C_F$  and  $C_A$  are quadratic Casimir invariants. For  $SU(3)$ ,  $C_F = 4/3$  and  $C_A = 3$ .  $C_F$ ,  $C_A$  and  $T_F$  are the colour factors associated to quark–gluon, gluon–gluon and quark–antiquark loops respectively as it is illustrated in Fig. 9.

In this way, the annihilation  $e^+e^- \rightarrow \gamma^*$ ,  $Z \rightarrow q\bar{q}$  is proportional to

$$\sum_{\text{colours}} \delta_{ij} \delta_{ji}^* = \text{tr}(\delta) = N_c. \quad (37)$$

In the Drell-Yan process, we must average over initial quark and antiquark colours, therefore

$$\sigma(q\bar{q} \rightarrow \gamma^*, Z \rightarrow l^+l^-) \propto 1/N_c. \quad (38)$$

In the same way, the deep inelastic scattering  $lq \rightarrow \gamma^*, Z \rightarrow lq$  cross section should be proportional to 1 because the sum over colour of the quarks in the final state is compensated by the average over the initial colour quark.

Finally, for the process  $\gamma^*, Z \rightarrow q\bar{q}g$  that gives rise to three jets, we have

$$\sum_{\text{colours}} |\mathcal{M}|^2 \propto \delta_{ij} t_{jk}^a (t_{lk}^a \delta_{il})^* = \text{tr}(t^a t^a) = \frac{1}{2} \text{tr}(\delta) = 4. \quad (39)$$

Notice that the multi particle production structure in  $e^+e^- \rightarrow \text{hadrons}$  is in jets a consequence of asymptotic freedom. In fact, the process is via the intermediate  $\gamma$  or  $Z$  that produces a quark–antiquark pair. This pair evolves as a colour singlet object, emitting gluons that in turn give rise to gluons or new quark–antiquark pairs, recombining at the end of the cascade to produce the observed hadrons in the final state. On the other hand, the probability that a quark emits a gluon at large transverse momentum (Fig. 10) is smaller than the probability of emitting a gluon of small transverse momentum due to asymptotic freedom that tells us that  $\alpha_s(|p - p'|^2)$  decreases for large  $|p - p'|^2$ . Therefore, the largest probability is for the emission of collimated gluons along the directions of the quark and the antiquark, forming two collimated jets. The existence of jets was proved by Sterman and Weinberg [15].

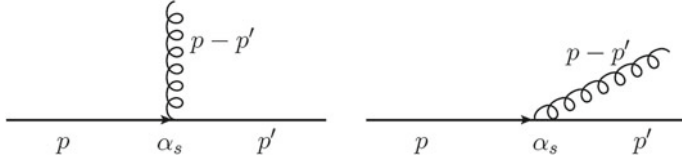


**Fig. 10** Diagrams for gluon emission

## 6 Symmetries

### 6.1 Isospin Symmetry

Let us consider QCD for  $u$  and  $d$  quarks. In the limit of equal masses, the QCD lagrangian is invariant under the transformations

$$\begin{aligned} u &\longrightarrow \alpha u + \beta d, \\ d &\longrightarrow \gamma u + \delta d, \end{aligned} \quad V = \begin{pmatrix} \alpha & \beta \\ \gamma & \delta \end{pmatrix}, \quad \det V = 1, \quad (40)$$

i.e.  $V \in SU(2)$ .

$u$  and  $d$  are isospin doublets (the rest of the quarks  $s, c, b, t$ , are isospin singlets). Actually,  $m_u < m_d$  and isospin is only an approximate symmetry. We can write the mass term in the lagrangian as

$$m_u \bar{u}u + m_d \bar{d}d = \frac{1}{2}(m_u + m_d)(\bar{u}u + \bar{d}d) + \frac{1}{2}(m_d - m_u)(\bar{d}d - \bar{u}u). \quad (41)$$

The first term is also isospin invariant but the second term breaks the symmetry. The mass difference  $m_d - m_u$  plays the role of a parameter that breaks the symmetry. The fact that hadrons are in almost degenerate multiplets implies that the second term is a small perturbation and therefore  $m_d - m_u$  must be small.

### 6.2 Chiral Symmetry

Let us consider the QCD lagrangian for massless  $u$  and  $d$  quarks. Then, the lagrangian is not only symmetric under the isospin symmetry transformation but also under the chiral transformation [16]

$$\begin{pmatrix} u_R \\ d_R \end{pmatrix} \longrightarrow V_R \begin{pmatrix} u_R \\ d_R \end{pmatrix}, \quad \begin{pmatrix} u_L \\ d_L \end{pmatrix} \longrightarrow V_L \begin{pmatrix} u_L \\ d_L \end{pmatrix}, \quad V_R, V_L \in SU(2), \quad (42)$$

where  $u_R, d_R$  ( $u_L, d_L$ ) denote the right (left) helicity states of quarks  $u$  and  $d$ .

This mapping corresponds to the direct product of two isospin groups:  $SU(2)_L \times SU(2)_R$ . The generators of this group are the three isospin generator  $\mathbf{I}$  and the three chiral isospin generators  $\mathbf{I}_5$ . The symmetry implies that the components of  $\mathbf{I}(I^+, I^-, I^3)$  and  $\mathbf{I}_5(I_5^+, I_5^-, I_5^3)$  are conserved. For instance, for  $I^+$  and  $I_5^+$

$$\begin{aligned} I^+ &= \int d\mathbf{x} \bar{u} \gamma^0 d = \int d\mathbf{x} u^+ d, \\ I_5^+ &= \int d\mathbf{x} \bar{u} \gamma^0 \gamma_5 d = \int d\mathbf{x} u^+ \gamma_5 d, \end{aligned} \quad (43)$$

we have

$$\begin{aligned} \partial_\mu (\bar{u} \gamma^\mu d) &= i(m_u - m_d) \bar{u} d, \\ \partial_\mu (\bar{u} \gamma^\mu \gamma_5 d) &= i(m_u + m_d) \bar{u} \gamma_5 d, \end{aligned} \quad (44)$$

which vanish for  $m_u = m_d = 0$  (if  $m_u = m_d \neq 0$  i.e. isospin symmetry, only the first equation of (44) vanishes).

Chiral symmetry must be spontaneously broken as pointed out by Nambu [17]. In fact, we observe that in the case of isospin symmetry: (a) The energy levels are degenerate forming multiplets i.e. hadrons are grouped into multiplets of equal mass; (b) The operators  $\mathbf{I}$  connect hadrons within the same multiplet—for instance, a neutron is transformed into a proton by  $I^+$ ,  $I^+|n\rangle = |p\rangle$ ; (c) The ground state  $|\Omega\rangle$  is an isospin singlet,  $\mathbf{I}|\Omega\rangle = 0$ .

If chiral symmetry takes place in the same way, the states should be grouped in degenerate multiplets of  $SU(2)_L \times SU(2)_R$ . As  $\mathbf{I}_5$  has negative parity, for each isospin multiplet it should exist a multiplet with the same mass and opposite parity. This is not seen in nature. For instance, the partners of the multiplet  $|n\rangle, |p\rangle$  are  $\mathbf{I}_5|n\rangle, \mathbf{I}_5|p\rangle$  that have opposite parity to neutron and proton. No such states exist.

If the vacuum is invariant under the action of any element of a given group  $G$ , we have

$$S|\Omega\rangle = e^{i\varepsilon Q}|\Omega\rangle \simeq (1 + i\varepsilon Q)|\Omega\rangle = |\Omega\rangle, \quad (45)$$

therefore

$$Q|\Omega\rangle = 0. \quad (46)$$

In our case

$$\mathbf{I}|\Omega\rangle = 0 \quad (47)$$

but

$$\mathbf{I}_5|\Omega\rangle \neq 0. \quad (48)$$

The vacuum breaks the symmetry (i.e. the symmetry is spontaneously broken). As

$$[\mathcal{L}_{QCD}, \mathbf{I}_5] = 0, \quad (49)$$

the three states  $\mathbf{I}_5|\Omega\rangle$  have the same energy as  $|\Omega\rangle$ . On the other hand, as  $|\Omega\rangle$  has zero momentum and  $\mathbf{I}_5$  carries no momentum,  $\mathbf{I}_5|\Omega\rangle$  must have zero momentum. Therefore, there will be three massless particles. indeed, on general grounds the Goldstone theorem [18] tells us that a spontaneously broken symmetry gives rise to a number of massless particles equal to the number of generators of the symmetry that become broken. The quantum numbers of  $\mathbf{I}_5|\Omega\rangle$  are spin  $\mathbf{S} = 0$ , negative parity  $P = -1$  and isospin  $\mathbf{I} = 1$  that are just the quantum numbers of the isospin triplet  $\pi^+$ ,  $\pi^0$ ,  $\pi^-$ . Therefore, it is natural to identify

$$I_5^+|\Omega\rangle = |\pi^+\rangle, \quad I_5^3|\Omega\rangle = |\pi^0\rangle, \quad I_5^-|\Omega\rangle = |\pi^-\rangle \quad (50)$$

as the three Goldstone bosons.

Note that  $I_5^+|n\rangle$  is not a singlet state partner of the neutron  $|n\rangle$  but the composed state formed by a positive pion and a neutron  $|\pi^+\rangle|n\rangle$  is.

Actually  $m_u, m_d \neq 0$  and therefore the chiral symmetry of the lagrangian is explicitly broken due to the mass term. We can split the hamiltonian in an invariant part  $\mathcal{H}_0$  and the mass term,

$$\begin{aligned} \mathcal{H} &= \mathcal{H}_0 + \mathcal{H}_{sb}, \quad \mathcal{H}_{sb} = \int d\mathbf{x} (m_u \bar{u}u + m_d \bar{d}d), \\ [\mathcal{H}_0, \mathbf{I}] &= 0 = [\mathcal{H}_0, \mathbf{I}_5]. \end{aligned} \quad (51)$$

Note that the quarks  $s, c, b, t$  are singlets and their mass do not break the symmetry. They are included in  $\mathcal{H}_0$ .

On the other hand, as

$$\langle \pi^+ | \bar{u} \gamma^\mu \gamma^5 d | 0 \rangle = -i p^\mu \sqrt{2} F_\pi e^{i p \cdot x} \quad (52)$$

and

$$\langle \pi^+ | \bar{u} \gamma^5 d | 0 \rangle = i \sqrt{2} G_\pi e^{i p \cdot x}, \quad (53)$$

where  $F_\pi$  is the axial coupling fixed by the decay width  $\pi^+ \rightarrow \mu^+ \nu$ ,  $\Gamma \propto F_\pi^2$ , and  $G_\pi$  the pseudo scalar coupling. As the second of (44), known as partially conserved axial current (PCAC), relates the matrix elements of (52) and (53), we obtain

$$m_\pi^2 = (m_u + m_d) \frac{G_\pi}{F_\pi}. \quad (54)$$

The (54) shows that for massless  $u$  and  $d$  quarks (chiral symmetry),  $m_\pi = 0$ . We observe that the pion mass does not depend linearly on the quark masses but quadratically.

### 6.3 Scale Symmetry and the Trace Anomaly

Under the mapping

$$x \longrightarrow \lambda x, \quad \psi_q \longrightarrow \lambda^{3/2} \psi_q, \quad G_\mu^a \longrightarrow \lambda G_\mu^a, \quad (55)$$

the QCD lagrangian is invariant for massless quarks. This symmetry is broken by quantum corrections introduced in the renormalisation process that always includes a scale. Therefore, we have a symmetry at the classical level that is broken by quantum corrections—an anomaly.

The current associated to the transformation is  $s^\mu = T^{\mu\nu} x_\nu$ , where  $T^{\mu\nu}$  is the energy-momentum tensor. Its divergence satisfies

$$\partial_\mu s^\mu = T_\mu^\mu = \frac{\beta(g_s)}{2g_s} F_{\mu\nu}^a F^{\mu\nu a} + [1 + \gamma(g_s)] m_q \bar{\psi}_q \psi_q, \quad (56)$$

where  $\beta$  and  $\gamma$  are the functions defined in (26) and (27).

$T_\mu^\mu$  is the trace of the energy-momentum tensor, playing a very important role at finite temperatures, because

$$T_\mu^\mu = \varepsilon - 3p \quad (57)$$

with  $\varepsilon$  and  $p$  the energy and pressure density respectively. The equation of state for any free gas is  $\varepsilon = 3p$  and  $T_\mu^\mu$  vanishes. Lattice QCD shows that  $T_\mu^\mu$  presents a maximum at a critical temperature  $T_c$ , marking the phase transition from a confined to a deconfined phase.

### 6.4 Vacuum Structure and Instantons

#### 6.4.1 The Vacuum in Quantum Mechanics: Instantons

Let us consider a periodic potential (Fig. 11). Classically, there are infinite degenerate ground states, each state corresponding to the particle sitting at rest at the positions  $x_n = na$ ,  $n = 0, \pm 1, \dots$  Quantum mechanically, if the barrier between each well is large enough, the classical ground states will correspond to Gaussian functions centered at  $x_n$ , having each an energy  $\hbar\omega/2$ .

A linear superposition

$$\psi(x) = \sum_n c_n \psi(x - x_n) \quad (58)$$

is again a ground state with energy  $\hbar\omega/2$ . The periodic symmetry implies that if  $\psi(x)$  is a solution,  $\psi(x + a)$  must be a solution. Hence, the solutions must have a



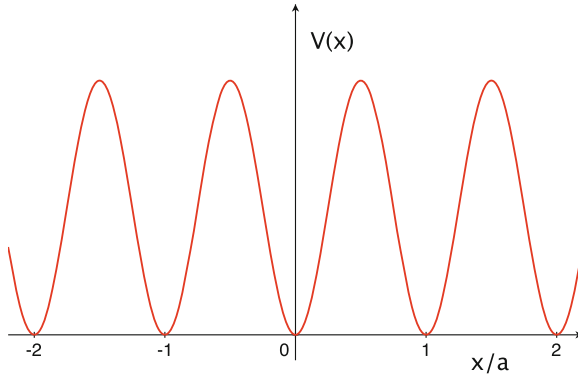


**Fig. 11** Scheme of a potential with multiple degenerate vacuums

shape  $e^{i\theta} \psi(x)$  and therefore  $c_n = e^{in\theta}$ . In this way, we write the equation

$$|\theta\rangle = \sum_n e^{in\theta} |n\rangle. \quad (59)$$

The quantum tunnelling between the states  $|n\rangle$  breaks the degeneracy of the state  $|\theta\rangle$  and the one corresponding to the minimal energy will be the ground state.

A very simple example of this is the wells represented in Fig. 12. The height of the central barrier is  $V_0/g$ . Doing  $g \rightarrow 0$ , there is an infinite barrier. In this case the ground state is doubly degenerate with energy  $E_0$ . For  $g \neq 0$ , there is tunnelling and the degeneracy is broken. The corresponding states  $|\Theta\rangle$  now are

$$\psi_{\pm} = \frac{1}{\sqrt{2}} [\psi(x - b - l) \pm \psi(x + b + l)] \quad (60)$$

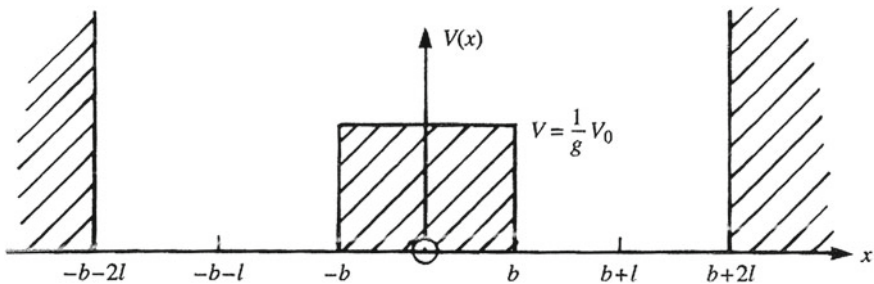


**Fig. 12** Two symmetric wells separated by a barrier. (Taken from the book by Leader and Predazzi [8])

corresponding to the energies  $E_{\pm}$  with

$$\Delta E = E_- - E_+ \simeq \frac{4\hbar E_0 \sqrt{g}}{l\sqrt{2mV_0}} \exp \left[ -\frac{2b}{\hbar} \sqrt{\frac{2mV_0}{g}} \right]. \quad (61)$$

Note that  $\Delta E$  is not analytic at  $g = 0$  and therefore cannot be obtained perturbatively.

In the path integral formalism the transition amplitudes are evaluated by the expression  $\exp[iS(x)/\hbar]$  summing over all possible paths  $x(t)$  contributing to the classical action  $S(x(t))$ , adding the contributions from paths obtained by small perturbations. However, in the case of transition amplitudes through barriers there is no classical path. In order to compute it, times  $t_1, t_2$  are continued to imaginary values  $-i\tau_1, -i\tau_2$ , so that the exponent becomes

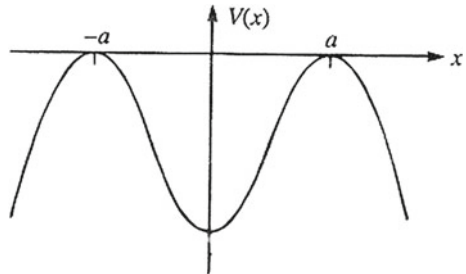
$$\begin{aligned} \frac{i}{\hbar} S(x)|_{t_1=-i\tau_1}^{t_2=-i\tau_2} &= \frac{i}{\hbar} \int_{-i\tau_1}^{-i\tau_2} dt \left[ \frac{1}{2m} \left( \frac{dx}{dt} \right)^2 - V(x) \right] \\ &= \frac{1}{\hbar} \int_{\tau_1}^{\tau_2} d\tau \left[ -\frac{1}{2m} \left( \frac{dx}{d\tau} \right)^2 - V(x) \right] = -\frac{1}{\hbar} S_E(x)|_{\tau_1}^{\tau_2}, \end{aligned} \quad (62)$$

where  $S_E$ , called the Euclidean action, is

$$S_E(x)|_{\tau_1}^{\tau_2} = \int_{\tau_1}^{\tau_2} d\tau \left[ \frac{1}{2m} \left( \frac{dx}{d\tau} \right)^2 + V(x) \right], \quad (63)$$

which is the action for a potential  $-V(x)$  such as shown in Fig. 13. What was a barrier has become a well, so that classical paths will now exist connecting  $x_1$  at  $\tau_1$  with  $x_2$  at  $\tau_2$ .  $\Delta E$  can be obtained computing the transition amplitude  $\langle x_1 = a, t = T | x_2 = a, t = 0 \rangle$  in the limit  $T \rightarrow \infty$  that will be dominated by the classical paths in the “mirror” problem. These classical paths are peculiar. In fact, it takes an infinitely long time to reach  $a$  because the potential is flat at  $-a$  and  $a$ , hence the velocity at these points is close to zero. Thus, the particles at rest for an infinite time and for a

**Fig. 13** Potential for the Euclidean problem. (Taken from the book by Leader and Predazzi [8])



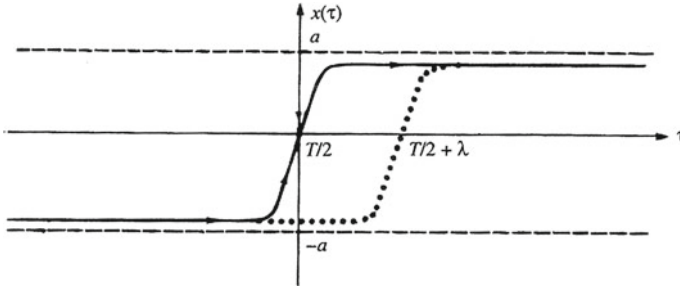


**Fig. 14** Trajectories of the instanton in Euclidean time: minimum (*solid*) and nearby trajectories (*dotted*). (Taken from the book by Leader and Predazzi [8])

short time it moves fast. The form of a classical path is shown in Fig. 14. A particle moving in this way is called instanton because its kinetic energy is non-zero only for a very short time. The Euclidean action is a minimum for an instant path and there will be infinite paths as the dotted line shown in Fig. 14, that differ from the one of the instant on only over a finite region of time. The sum of all will give an important contribution.

#### 6.4.2 The QCD Vacuum

Let us consider the gauge matrix  $G_\mu(x) = T^a G_\mu^a(x)$  and take  $G_\mu^a(x) = 0$ . The spatial components of the gauge matrix transform as

$$\mathbf{G} \rightarrow U \mathbf{G} U^{-1} + \frac{i}{g} (\nabla U) U^{-1}, \quad (64)$$

with

$$U = \exp(-iT^a \mathbf{G}^a). \quad (65)$$

The field energy is zero when  $\mathbf{G} = 0$  and therefore it will be zero when  $\mathbf{G}$  is a pure gauge,

$$\mathbf{G} = \frac{i}{g} (\nabla U) U^{-1}, \quad (66)$$

because they are each other related to the gauge transformation (64).

In order to see the degeneracy of the ground state we are going to use  $SU(2)$  instead of  $SU(3)$  for simplicity. For  $SU(2)$ , the generators are proportional to the Pauli matrixes, so that the gauge transformations (65) become

$$U = \exp(-i\boldsymbol{\sigma} \cdot \boldsymbol{\theta}(x)/2). \quad (67)$$

In general, they do not have an angle independent limit as  $r \rightarrow \infty$ , hence we can write the more restrictive form

$$U = \exp(-i \boldsymbol{\sigma} \cdot \mathbf{r} f(r)/r) = I \cos f(r) + i \frac{\boldsymbol{\sigma} \cdot \mathbf{r}}{r} \sin f(r) \quad (68)$$

that will be independent of the angles for  $r \rightarrow \infty$  provided  $\sin f(r) = 0$  as  $r \rightarrow \infty$  or

$$\lim_{r \rightarrow \infty} f(r) = n\pi \quad (69)$$

which implies  $\lim_{r \rightarrow \infty} U(\mathbf{r}) = \pm I$ .

We also require that  $f(0) = 0$  for  $U(\mathbf{r})$  to be a single valued functions at  $r = 0$ .

The gauge transformations (68) can be classified into subsets, labelled by an integer  $n$ ,

$$U_n(\mathbf{r}) = \exp(-i \boldsymbol{\sigma} \cdot \mathbf{r} f_n(r)/r), \quad (70)$$

with  $f_n(\infty) = n\pi$ . A given gauge transformation of one class cannot be continuously deformed into another gauge transformation of another class.

The gauge transformation class (70) satisfies

$$n = \frac{1}{24\pi^2} \int d\mathbf{r} \varepsilon_{ijk} \text{tr}\{(U \partial_i U^{-1})(U \partial_j U^{-1})(U \partial_k U^{-1})\}. \quad (71)$$

The integer  $n$  is called the winding number or the topological charge that labels the gauge transformation classes, called homotopy classes.

In summary, the classical theory has degenerate vacuum states (with zero energy) labelled by the winding numbers  $n$ , corresponding to pure gauge configurations

$$\mathbf{G}_n = \frac{i}{g} (\nabla U_n) U_n^{-1}. \quad (72)$$

In the semiclassical approximation to quantum QCD, the vacuum will be

$$|\theta\rangle = \sum e^{in\theta} |\mathbf{G}_n\rangle, \quad (73)$$

where the states  $|\mathbf{G}_n\rangle$  are eigenstates of the matrix gauge operators  $\mathbf{G}_n$  that have the values corresponding to the ground state of winding number  $n$ .

Similarly to the one-dimensional period potential, there is tunnelling between the states  $|\mathbf{G}_n\rangle$ . This tunnelling is generated through the existence of instanton configurations of the gauge matrix  $\mathbf{G}_n(\tau, \mathbf{r})$  with  $n$  integer that correspond to a finite Euclidean action, being solutions of the classical field equations in the Euclidean space having essentially zero Euclidean field energy and evolving from  $\mathbf{G}_n(\mathbf{r})$  at  $\tau \rightarrow -\infty$  to  $\mathbf{G}_{n+n'}(\mathbf{r})$  at  $\tau \rightarrow +\infty$ .

The Euclidean action is given by

$$S_E = \frac{1}{2} \int d\tau d\mathbf{r} \operatorname{tr}(F_{\alpha\beta}^{aE} F_{\alpha\beta}^{aE}) = \frac{1}{2} \int d\tau d\mathbf{r} \operatorname{tr}(F_{\mu\nu}^a F^{\mu\nu a}), \quad (74)$$

where  $\alpha, \beta$  are Euclidean indices ( $x, y, z, it$ ) and  $F_{ij}^E = -F^{ij}$ ,  $F_{4j}^E = -iF^{0j}$ .

Now

$$\mathbf{G}_\mu \longrightarrow_{R \rightarrow \infty} -\frac{i}{g} (\partial_\mu U) U^{-1}, \quad (75)$$

with  $R = \sqrt{\tau^2 + r^2}$ .

From a similar formula to (71) it is obtained

$$n = -\frac{g^2}{16\pi^2} \int d\tau d\mathbf{r} \operatorname{tr}(F_{\alpha\beta}^{aE} F_{\alpha\beta}^{aE}) = -\frac{g^2}{16\pi^2} \int d\tau d\mathbf{r} \operatorname{tr}(F_{\mu\nu}^a F^{\mu\nu a}). \quad (76)$$

Defining the current

$$K^\mu \equiv 2\varepsilon^{\mu\nu\rho\sigma} \operatorname{tr} \left( \mathbf{G}_\nu^a \partial_\rho \mathbf{G}_\sigma^a - \frac{2}{3} i g f_{abc} \mathbf{G}_\nu^a \mathbf{G}_\rho^b \mathbf{G}_\sigma^c \right), \quad (77)$$

it is observed that

$$\partial_\mu K^\mu = \operatorname{tr}(\tilde{F}_{\mu\nu} \tilde{F}^{\mu\nu}), \quad (78)$$

where the dual tensor  $\tilde{F}_{\mu\nu}$  is defined by

$$\tilde{F}_{\mu\nu} = \frac{1}{2} \varepsilon_{\mu\nu\gamma\delta} F_{\gamma\delta}. \quad (79)$$

Introducing (78) in (76) and using the Gauss theorem, we get

$$n = -\frac{g^2}{16\pi^2} \int d\tau d\mathbf{r} \partial_\alpha^E K_\alpha^E = -\frac{g^2}{16\pi^2} \int_{r=\infty} dS_\alpha K_\alpha^E \quad (80)$$

( $K_4^E = iK^0$ ,  $K_j^E = K^j$ ), where the last integral is extended to the three dimensional surface  $R = \infty$ . At this surface, the finite action configurations are pure gauge, then using (75) and (77) we recover (71).

Note that in the evaluation of the probability amplitude to go from the ground state in  $t_1$  to the ground state in  $t_2$  we will have, going to imaginary time,

$$\langle \theta | e^{-\mathcal{H}(\tau_2 - \tau_1)} | \theta \rangle = \sum_{n,m} e^{i(n-m)\theta} \langle \mathbf{G}_m | e^{-\mathcal{H}(\tau_2 - \tau_1)} | \mathbf{G}_n \rangle. \quad (81)$$

Hence, there is need to compute

$$e^{i(n-m)\theta} \exp[-S_E] = \exp \left\{ - \int d\tau d\mathbf{r} \left[ \mathcal{L} - i\theta \frac{g^2}{16\pi^2} \text{tr}(F_{\alpha\beta}^{aE} F_{\alpha\beta}^{aE}) \right] \right\}, \quad (82)$$

which is equivalent to work with the new lagrangian density

$$\mathcal{L}_\theta = \mathcal{L} + \theta \frac{g^2}{32\pi^2} F_{\mu\nu}^a \tilde{F}^{a\mu\nu}. \quad (83)$$

This new term violates  $CP$  invariance. Experimental data as the electric dipole moment of the neutron implies a very small number for  $\theta$ ,  $\theta < 10^{-10}$ . Why this small value? This is known as the QCD  $CP$  problem. There are several proposals to answer this question, including the existence of a new particle, the axion, whose field is associated to  $\theta$  [19, 20].

A detailed discussion of all these aspects can be found in the book by Leader and Predazzi in [8].

### 6.4.3 $U_A(1)$ Symmetry and the Axial Anomaly

The QCD lagrangian is invariant under the  $U(1)$  transformations

$$\psi_q \rightarrow e^{i\alpha} \psi_q, \quad \bar{\psi}_q \rightarrow e^{i\alpha\gamma_5} \bar{\psi}_q. \quad (84)$$

If the chiral transformation is spontaneously broken, there will be a massless Goldstone boson with  $I = 0$  and  $P = -1$ . The lightest pseudo scalar with  $I = 0$  is the  $\eta$  whose mass is  $549 \text{ MeV}/c^2$ , much larger than the pion mass. Therefore the symmetry is not spontaneously broken. This is the  $U_A(1)$  problem. We discuss a way out [21, 22].

The symmetry under the chiral  $U_A(1)$  gives rise to the current

$$j_{\mu 5}^0 = \bar{u} \gamma_\mu \gamma_5 u + \bar{d} \gamma_\mu \gamma_5 d \quad (85)$$

(we are considering two flavours  $u$  and  $d$  and the  $I = 0$  content as the superscript indicates).

This current is conserved classically but not in a quantised theory, where

$$\partial^\mu j_{\mu 5}^0 = N_f \frac{g^2}{8\pi^2} F_{\mu\nu}^a \tilde{F}^{a\mu\nu}. \quad (86)$$

If we define the current

$$\tilde{j}_{\mu 5} = j_{\mu 5}^0 - N_f \frac{g^2}{8\pi^2} K_\mu, \quad (87)$$

it is obviously conserved,

$$\partial^\mu \tilde{j}_{\mu 5} = 0. \quad (88)$$

Let us consider the charges associated to these currents,

$$\begin{aligned} q_5(t) &= \int d\mathbf{r} j_{05}^0(t, \mathbf{r}), \\ Q_5(t) &= \int d\mathbf{r} \tilde{j}_{05}(t, \mathbf{r}). \end{aligned} \quad (89)$$

$q_5$  is gauge invariant but it is not time independent because  $j_{\mu 5}^0$  is not conserved.  $Q_5$  is conserved but it is not invariant under gauge transformations of a given class  $U_n$ ,

$$Q_5 \rightarrow U_n Q_5 U_n^{-1} = Q_5 + 2nN_f \quad (90)$$

or  $[U_n, Q_5] = 2nN_f U_n$ . Now, we have

$$[\mathcal{H}, U_n] = 0, \quad [\mathcal{H}, Q_5] = 0, \quad [U_n, Q_5] \neq 0 \quad (91)$$

and, therefore, we cannot diagonalise simultaneously  $\mathcal{H}$ ,  $U_n$  and  $Q_5$ . The vacuum  $|\theta\rangle$  is an eigenstate of  $\mathcal{H}$  and  $U_n$  but not of  $Q_5$ . Thus, the vacuum is not chiral invariant and  $U_A(1)$  is not a symmetry due to the transition between instantons [21],

$$e^{-i\phi Q_5} |\theta\rangle = |\theta + 2N_f \phi\rangle. \quad (92)$$

## 7 The QCD Phase Diagram

Forty years ago, Lee and Wick [23] pointed out the possibility of studying new Physics by exploring the behaviour of high density matter or high energy density in a volume. In this way, it would be possible the restoration of broken symmetries, to disturb the the vacuum and the creation of abnormal dense matter. Also, it was very early realised [24–29] that asymptotic freedom should imply the existence of very high density matter formed by deconfined quarks and gluons. Later, these deconfined quarks and gluons, if thermalised, were referred to as Quark–Gluon Plasma (QGP). It would be expected a phase transition between normal nuclear matter and deconfined quarks and gluons because of the large difference in the number of degrees of freedom. In fact, the energy density for a gas of free pions is

$$\varepsilon_{\text{HG}} = \frac{\pi^2}{30} 3 T^4 \simeq T^4, \quad (93)$$

whereas for a gas of free quarks and gluons is

$$\varepsilon_{\text{QGP}} = \frac{\pi^2}{30} \left[ 2 \times 8 + \frac{7}{8} \times 2(3) \times 2 \times 2 \times 3 \right] T^4 = \frac{\pi^2}{30} [16 + 21(31.5)] T^4 \quad (94)$$

where we take into account that each of the 8 gluons has 2 helicities, and the 2(3) quark flavours may have 2 helicities, 3 possible colours and an additional factor 2 takes into account antiquarks. In (93) and (94) we neglect the masses, because their inclusion changes only slightly the formulae.

The energy density as a function of the temperature has been studied in lattice QCD with two and three light quarks and in the more realistic situation of two light and one heavier quark. Figure 15 shows that in a very narrow temperature interval there is rapid increase from the low values of hadronic matter to much higher values as it was expected in the transition from confined to deconfined quarks and gluons. It is observed that even for  $T > T_c$  the lattice values are much lower than the values given by (94), 12.25 and 15.61 for the cases of 2 and 3 flavours respectively. This result points out that for moderate temperatures the deconfined quarks and gluons go on interacting strongly. It is denoted by strongly coupled QGP (scQGP). The transition seems to be a cross-over (fast change but without discontinuity) although this depends on the number of flavours used in the simulation and on the masses [30].

At deconfinement, the quark–antiquark binding is dissolved so that the conventional hadrons melt. However, the pions would persist beyond this point unless chiral symmetry is restored here. A measure of chiral symmetry breaking is provided by the quark mass term  $\langle \bar{\psi} \psi \rangle$ : if  $\neq 0$ , the chiral symmetry of the lagrangian is spontaneously broken. The chiral order parameter (condensate) is defined by

$$K(T) = \langle \bar{\psi} \psi \rangle = \frac{T}{V} \left( \frac{\partial \ln Z(T, m_q)}{\partial m_q} \right)_{m_q=0}. \quad (95)$$

**Fig. 15** Energy density as a function of temperature in lattice QCD [31, 32]. From bottom to top the results are for two light flavours, three light flavours and two light and one heavy flavour. Arrows on the right side indicate the corresponding results for an ideal gas according to the Stefan-Boltzmann law

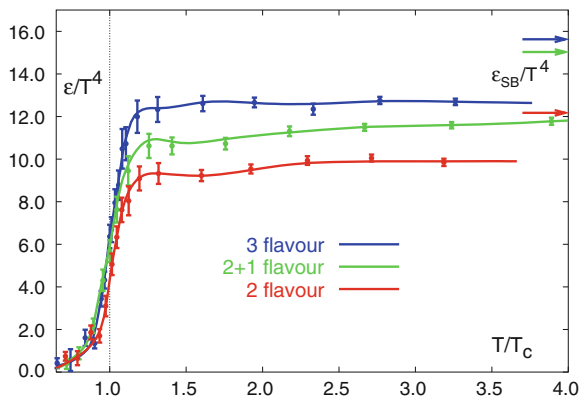
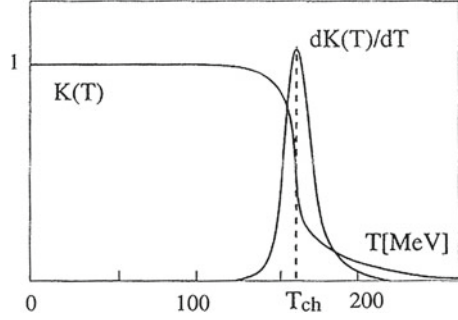




**Fig. 16** Temperature dependence of the chiral condensate and of the corresponding susceptibility. (Taken from [30])



The behaviour of  $K(T)$  in the case of two light (u,d) and one heavy (s) quark is shown in Fig. 16, with a sharp change at a critical temperature  $T_c \simeq 160$  MeV. This temperature coincides with the critical temperature found in the deconfinement transition.

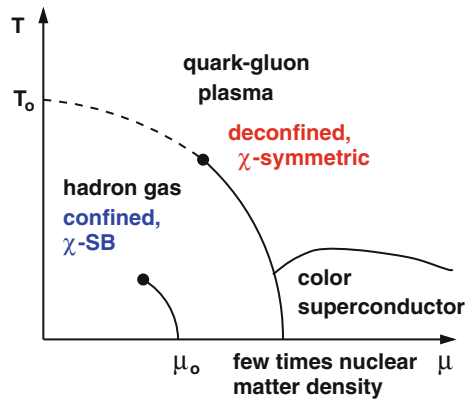
The results of lattice QCD for higher baryon density and low temperature point out to the existence of a first order phase transition. As at high temperature and lower baryon density the transition is just a cross-over, a critical point should exist as shown in Fig. 17.

The energy density reached in central (i.e. at impact parameter  $b = 0$ ) nucleus-nucleus collisions can be evaluated using the Bjorken formula [33]

$$\varepsilon = \frac{\langle p_T \rangle}{\tau_0 \pi R_A^2} \frac{dN/dy}{R_A^2}. \quad (96)$$

Here  $dN/dy$  denotes the number of particles produced in central rapidity,  $\langle p_T \rangle$  the mean transverse momentum,  $R_A$  the nuclear radius and  $\tau_0 = 1$  fm/c is the time after the collision when the energy density is evaluated.

**Fig. 17** Phase diagram of QCD obtained in lattice for 3 quarks [31]. *Solid lines* indicate a first order phase transition, *dashed* ones a cross-over and the *dots* indicate critical points



At the highest energies studied at the Super Proton Synchrotron (SPS) at CERN and at the Relativistic Heavy-Ion Collider (RHIC) at BNL for PbPb (SPS) and AuAu (RHIC) collisions, the values of the energy density are larger than 2 and 4 GeV/fm<sup>3</sup> respectively. At the Large Hadron Collider (LHC) at CERN, for PbPb collisions at 2.76 TeV/nucleon, the value of the energy density is larger than 15 GeV/fm<sup>3</sup>. In all cases the values are above the critical energy determined in lattice QCD, 0.5 GeV/fm<sup>3</sup>.

Besides, lattice QCD has studied the behaviour of the pressure density, as shown in Fig. 18, and  $(\varepsilon - 3p)/T^4$ , shown in Fig. 19, related to the trace anomaly. It can be seen that  $(\varepsilon - 3p)/T^4$  above the critical temperature decreases slowly in such a way that it has a sizeable value even for  $T \simeq 3 - 4 T_c$ . Therefore, even at those temperatures we are far from an state of free quarks and gluons whose equation of state is  $\varepsilon = 3p$ .

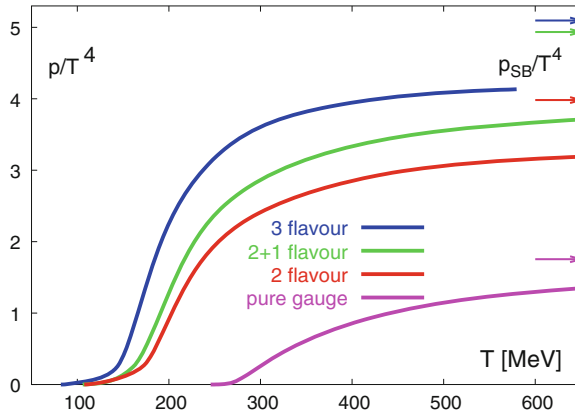


**Fig. 18** Pressure versus temperature obtained in lattice QCD [31]. Lines from bottom to top indicate the results for 0, 2 light, 2 light and 1 heavy, and 3 light quarks. Arrows on the right side indicate the corresponding results for an ideal gas according to the Stefan-Boltzmann law

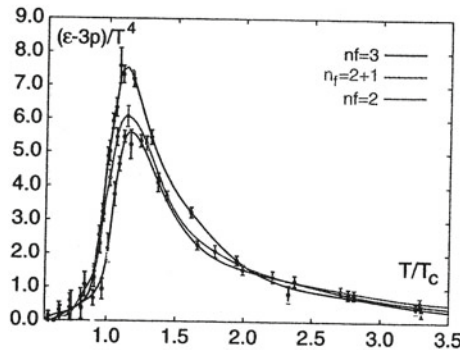


**Fig. 19** Interaction measure from lattice QCD, for 2 light, 2 light and 1 heavy, and 3 light quarks. (Taken from [30])

In the last decades there has been much experimental activity concerned with the obtention and study of the high density state of quarks and gluons. First, the Intersecting Storage Rings (ISR) at CERN and the Alternating Gradient Synchrotron (AGS) at BNL explored collisions between light nuclei and at not very high energies. Later, the SPS experiments at 20 GeV/nucleons and RHIC at 62.4 and 200 GeV/nucleon studied extensively a broad range of collisions, centralities and observables. Now the LHC has collided PbPb (also pPb) at 2.76 TeV/nucleon and will reach even higher energies soon. There are many interesting and exciting phenomena seen in these experiments [34–40]: Strong suppression of high  $p_T$  particles in nucleus-nucleus relative to the number obtained from nucleon–nucleon collisions scaled by the number of binary collisions; Suppression of back-to-back correlations in jet production (jet quenching); Elliptic flow of particles whose behaviour is consistent with hydrodynamical evaluations assuming that the partonic system created in the collision becomes isotropic in a short time after the collision, and this partonic system has a very low shear viscosity over entropy density value; Sequential melting of bottomium states according to their binding energy and size, such as expected due to deconfinement and colour screening—related to this, it has been observed an interesting behaviour of the suppression of the  $J/\psi$  and the charmonium resonances; Rapidity long range correlations and ridge structure in the two particle correlations. All these phenomena point out to the existence of an initial state with saturated gluons close to a thermalised state with a collective flow similar to a liquid of a very low shear viscosity. Due to the formation of this high density partonic medium, the propagation of particles with large  $p_T$  is strongly modified compared to the propagation in vacuum.

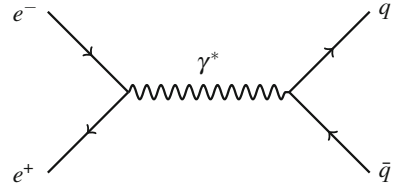
## 8 Phenomenological Applications of Perturbative QCD

In this Section we address the most important evidences of QCD as the theory of the strong interactions in the perturbative domain. Complete information and details on the subjects treated here can be found in [3, 41].

### 8.1 $e^+e^-$ Annihilation into Hadrons

Let us consider the process of  $e^+e^-$  annihilation into hadrons at the lowest order in perturbation theory (leading order) i.e. at tree level, see Fig. 20. We neglect electro-weak corrections ( $Z^0$  exchange) and consider the centre-of-mass frame and large energies  $E_{cm} \gg \Lambda_{QCD}$ . As hadronisation happens at scales of order  $\Lambda_{QCD}$ , while the production of the  $q\bar{q}$  pair happens at scales  $E_{cm}$ , in this situation they can be considered as decoupled and perturbation theory in terms of quarks and gluons is expected to give a good description of the physical process.

**Fig. 20** Feynman diagram for  $e^+e^- \rightarrow$  hadrons at tree level



The corresponding angular dependence of the cross section for the production of one shower of particles (called jet—see below, that comes from the radiation of a single quark or antiquark) reads

$$\frac{d\sigma}{d\cos\theta} = \frac{\pi\alpha_{em}^2 Q_f^2}{2E_{cm}^2} (1 + \cos^2\theta), \quad (97)$$

with  $Q_f$  the electric charge of the quarks with flavour  $f$ . The total cross section for production of quarks of a given colour and flavour obtained upon angular integration of (97) reads  $\sigma_0 = 4\pi\alpha_{em}^2 Q_f^2 / (3E_{cm}^2)$ , and the corresponding ratio

$$R = \frac{\sigma(e^+e^- \rightarrow \text{hadrons})}{\sigma(e^+e^- \rightarrow \mu^+\mu^-)} = \frac{\sum_f \sigma(e^+e^- \rightarrow q\bar{q})}{\sigma(e^+e^- \rightarrow \mu^+\mu^-)} = N_c \sum_f Q_f^2, \quad (98)$$

where  $N_c = 3$  is the number of colours. As commented before, the approximate description that this expression provides of experimental data is one of the evidences for the existence of 3 colours in Nature.

Now we turn to the next-to-leading (radiative) corrections in QCD to this process, that are  $\mathcal{O}(\alpha_s)$ . They can be classified into those that contain new real partons, called *real corrections*, and those that do not contain them but they participate in loops (*virtual corrections*). The corresponding amplitudes are given by the Feynman diagrams in Figs. 21 and 22 respectively.

The virtual corrections contain two types of divergencies. On the one hand, there are ultraviolet ones that are absorbed through the usual method of renormalisation into the redefinition of the fields and coupling constant. On the other hand, there are

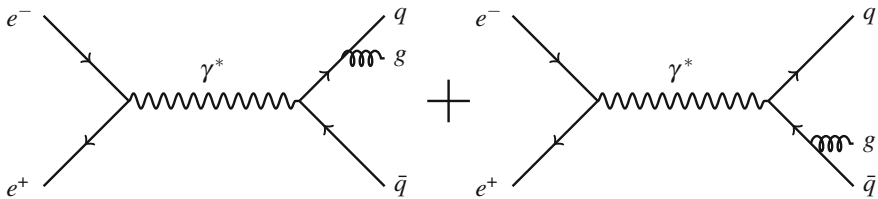


**Fig. 21** Feynman diagrams of the real next-to-leading corrections to  $e^+e^- \rightarrow$  hadrons

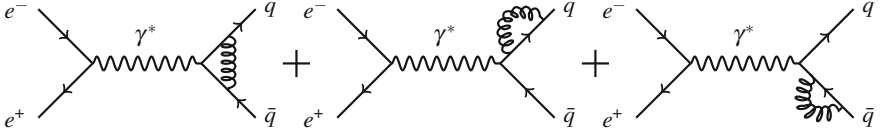


**Fig. 22** Feynman diagrams of the virtual next-to-leading corrections to  $e^+e^- \rightarrow \text{hadrons}$

infrared divergencies for massless quarks that come through integrals like

$$I = \int \frac{d^4k}{(2\pi)^4} \frac{1}{k^2 + i\varepsilon} \frac{1}{(p_1 + k)^2 - m^2 + i\varepsilon} \frac{1}{(p_2 - k)^2 - m^2 + i\varepsilon} \\ \sim \int \frac{d^4k}{(2\pi)^4} \frac{1}{k^2 2p_1 \cdot k (-2p_2 \cdot k)} \quad (99)$$

that presents a logarithmic divergency.

The real corrections contain two kinds of divergencies, collinear (or mass, see below) and infrared divergencies, when the emitted parton (gluon) is either collinear to the emitting parton or very soft. They are contained in the gluon emission probability given by the diagram in Fig. 23, that reads in the soft and collinear limit

$$dP \propto \frac{\alpha_s C_R}{\pi} \frac{dx}{x} \frac{dk_\perp^2}{k_\perp^2} \propto \frac{d\omega}{\omega} \frac{d\theta}{\theta}, \quad \theta \simeq \frac{k_\perp}{\omega}, \quad (100)$$

with  $C_R$  the quadratic Casimir of the colour representation of the emitting parton.

The singularities can be regularised using dimensional regularisation i.e. working in  $d = 4 - 2\varepsilon$  dimensions. The result for the real corrections reads

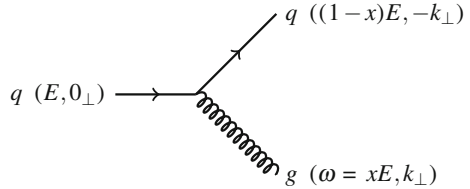
$$\sigma_{real} = \sigma_0 N_c \sum_f Q_f^2 \frac{\alpha_s C_F}{2\pi} H(\varepsilon) \left[ \frac{2}{\varepsilon^2} + \frac{3}{\varepsilon} + \frac{19}{2} + \mathcal{O}(\varepsilon) \right], \quad (101)$$

while that for the virtual ones

$$\sigma_{virtual} = \sigma_0 N_c \sum_f Q_f^2 \frac{\alpha_s C_F}{2\pi} H(\varepsilon) \left[ -\frac{2}{\varepsilon^2} - \frac{3}{\varepsilon} - 8 + \mathcal{O}(\varepsilon) \right], \quad (102)$$

with  $H(\varepsilon) = 1 + \mathcal{O}(\varepsilon)$ .

**Fig. 23** Feynman diagram giving the gluon emission probability off a quark, with the corresponding kinematical variables



The outcome of this calculation, of general applicability, is that soft divergencies cancel between virtual and real corrections. On the other hand, for sufficient inclusive quantities (e.g. for the total cross section where we sum over initial and final states and thus we cannot distinguish a quark from a quark plus a collinear gluon), collinear divergencies vanish, which is the Kinoshita-Lee-Nauenberg theorem. Thus, this observable is infrared and collinear (IRC) safe and can be computed reliably in perturbation theory. A comparison of data with theoretical calculation can be seen in Fig. 24.

On the other hand, the production of three jets through the emission of an energetic (hard) gluon, in  $e^+e^-$  annihilation, see Fig. 25, provides evidence of the existence of the gluon and also of its spin-1 nature. The angular distribution between the most energetic jet in the event and the other two reflects the spin of the emitted gluon, and experimental data clearly favour the spin-1 hypothesis over the spin-0 one. Besides, the existence of non-abelian vertices like  $ggg$  produce multi-jet angular distributions that are different from the purely abelian ones  $q\bar{q}g$ . Again, experimental data demand the existence of non-Abelian vertices and thus provide a test of the non-abelian nature of QCD.

Finally, both the multi-jet distributions and the value of  $R$  itself, which receive contributions from radiative corrections, are sensitive to the value and running of  $\alpha_s$  and thus allow one of the most precise determinations of this key quantity, see Fig. 7 and [43].

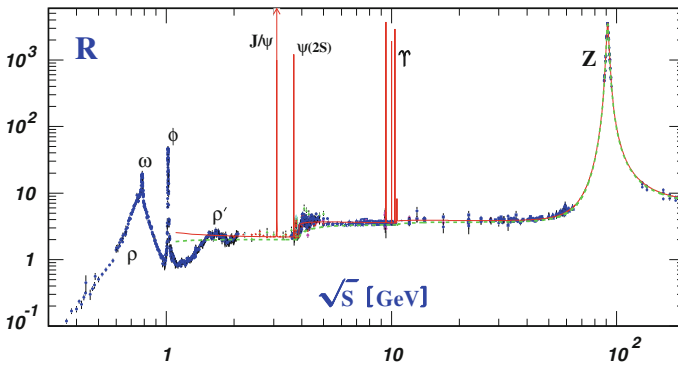


Fig. 24 Compilation of data on  $R$  compared to theoretical calculations. (Taken from [42])

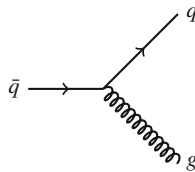
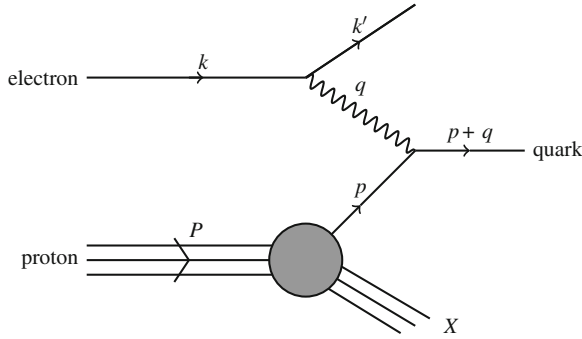


Fig. 25 Illustration of three jet production in  $e^+e^-$  annihilation. Each parton will produce a jet



**Fig. 26** Feynman diagram for DIS at lowest order in perturbation theory and considering just virtual photon exchange

## 8.2 Deep Inelastic Scattering

Here we address the analysis of a hadron through a Rutherford-type experiment: the hadron is bombarded by leptons, in a process that is known as Deep Inelastic Scattering (DIS), see Fig. 26. The total cross section is determined by two variables: the scattering angle and the energy, of the outgoing lepton. The variables used to describe this process are

$$\begin{aligned}
 Q^2 &= -q^2, \\
 M^2 &= p^2, \\
 \nu &= p \cdot q = M(E - E'), \\
 x &= \frac{Q^2}{2\nu} = \frac{Q^2}{2M(E - E')}, \\
 y &= \frac{p \cdot q}{p \cdot k} = 1 - E'/E,
 \end{aligned} \tag{103}$$

where the last equalities in the three last lines hold in the reference frame in which the hadron is at rest.

For charged lepton scattering and neglecting electro-weak contributions (i.e.  $Z^0$  or  $W^\pm$  exchange), the electromagnetic cross section reads

$$\frac{d^2\sigma}{dx dy} = \frac{8\pi\alpha_{em}^2 ME}{Q^4} \left[ \frac{1 + (1-y)^2}{2} 2x F_1 + (1-y)(F_2 - 2x F_1) - \frac{M}{2E} xy F_2 \right], \tag{104}$$

where  $F_1$  and  $F_2$  are the structure functions of the hadron.

The comparison of this expression with the corresponding one for elastic scattering of a lepton on a point-like spin-1/2 particle and on an extended one, leads to the well known conclusions: (i) the experimental fact that, for fixed  $x$ ,  $F_1$  and  $F_2$  are

roughly independent of  $Q^2$  for large enough  $Q^2$ —*Bjorken scaling*—compared to the  $1/Q^4$  behaviour of the proton form factors, leads to the conclusion that the hadron is composed of point-like charged scatterers; and (ii) the experimental fact that  $2xF_1 \simeq F_2$ —*Callan-Gross relation*—implies that those scatterers are spin-1/2 particles.

Now, in a frame in which the hadron is moving very fast (the infinite momentum frame IMF), the hadron can be considered as an incoherent superposition of constituents, called partons. This is due to the fact that, for high enough  $Q$ , the scale of the interaction between partons,  $\Lambda_{QCD}$ , is much smaller than  $Q$ , and constitutes the basis of the *parton model* due to Bjorken, Feynman and Gribov.

In the parton model, the cross section for the DIS process shown in Fig. 26 can be written in the factorised form

$$\begin{aligned} \sigma[l(k) + \text{hadron}(P) \rightarrow l(k') + p + q + X] \\ = \int_0^1 d\xi \sum_f f(\xi) \sigma[l(k) + q_f(p = \xi P) \rightarrow l(k') + p + q], \end{aligned} \quad (105)$$

where  $f(\xi)$  represents the lower blob in Fig. 26 and can be interpreted as the probability of finding a parton  $q_f$  with momentum  $p = \xi P$  in the hadron (parton density function PDF), while  $\sigma[l(k) + q_f(p = \xi P) \rightarrow l(k') + p + q]$  is the cross section of this parton with the lepton and corresponds to the upper part of the Feynman diagram in the figure.

In the parton model

$$F_2(x) = 2xF_1(x) = \sum_f \int_0^1 d\xi f(\xi) x Q_f^2 \delta(x - \xi) = \sum_f Q_f^2 x f(x), \quad (106)$$

where the sum runs over all (anti)partons in the hadron. In this way, the variable  $x$  can be identified with the momentum fraction of the parton in the hadron. Furthermore, if the charged partons are identified with the quarks in the quark model, then

$$F_2^{eN}(x) = \frac{5}{18} F_2^{vN}(x), \quad F_2^{ep}(x) - F_2^{en}(x) = \frac{1}{3} x[u_v(x) - d_v(x)], \quad (107)$$

where  $N$  is either a proton  $p$  or a neutron  $n$ , and  $u_v$  and  $d_v$  are the PDFs for valence  $u$  and  $d$  quarks respectively. The experimental verification of these relations supported the identification of the partons in the parton model with the quarks in the quark model and in QCD. Finally, the experimental finding that

$$\int_0^1 dx F_2^{vN}(x) = \int_0^1 dx \sum_{\text{charged } f} x f(x) \simeq 0.44 \quad (108)$$



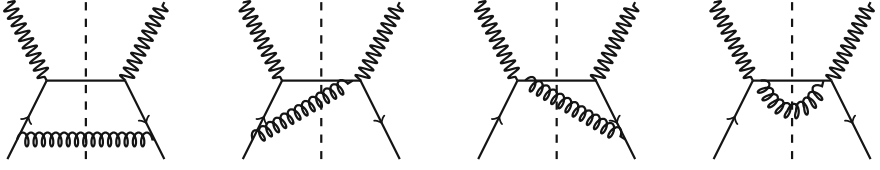


**Fig. 27** Squared amplitudes for the QCD corrections to the parton model in the DIS process. The *dashed vertical lines* correspond to the cut where the amplitude (to the *left* of the cut) and the complex conjugate amplitude (to the *right* of the cut) join. All cut particles are on-shell

lead to the conclusion that there is missing momentum in the charged sector of the hadrons, so there exist partons in the hadrons without electric charge, to be identified with the QCD gluons.

Now we turn to the QCD corrections to the parton model, due to the fact that partons: quarks and gluons, radiate. The squared diagrams for the DIS process are given in Fig. 27.

The only diagram that (in light-cone gauge) gives rise to (logarithmic) divergencies in the one on the left in Fig. 27. This logarithmic divergencies lead to an evolution of the parton densities, given by the Dokshitzer-Gribov-Lipatov-Altarelli-Parisi (DGLAP) evolutions equations, that read schematically

$$\frac{\partial f(x, Q^2)}{\partial \ln Q^2} = \frac{\alpha_s(Q^2)}{2\pi} \int_x^1 \frac{dz}{z} \sum_{f'} P_{f \leftarrow f'} \left( \frac{x}{z} \right) f'(z, Q^2), \quad (109)$$

where the sum runs over all partons  $f'$  that may produce parton  $f$  with momentum fraction  $x/z$ , with probability given by function  $P_{f \leftarrow f'} \left( \frac{x}{z} \right)$ , known as DGLAP splitting function. It is given by e.g. the diagram in Fig. 23, for the  $q \rightarrow g$  splitting function with  $x \rightarrow x/z$  and for the  $q \rightarrow q$  splitting function with  $1 - x \rightarrow x/z$ .

While the exact expressions of the evolutions equations and splitting functions (available up to next-to-next-to-leading order) can be found elsewhere, let us discuss their physical origin slightly more in depth. For that, consider both initial state real and virtual corrections to the DIS process, as shown in Figs. 28 and 29.

**Fig. 28** Feynman diagram for initial state real corrections to DIS at lowest order in perturbation theory

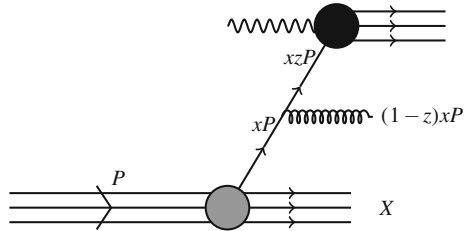
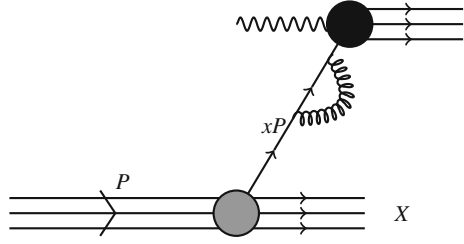


**Fig. 29** Feynman diagram for initial state virtual corrections to DIS at lowest order in perturbation theory



Both contributions are IR and collinearly divergent:

$$\sigma_{real} \simeq \sigma_h(xzP) \frac{\alpha_s C_F}{\pi} \frac{dz}{1-z} \frac{dk_{\perp}^2}{k_{\perp}^2}, \quad (110)$$

$$\sigma_{virtual} \simeq -\sigma_h(xP) \frac{\alpha_s C_F}{\pi} \frac{dz}{1-z} \frac{dk_{\perp}^2}{k_{\perp}^2}, \quad (111)$$

where  $\sigma_h$  denotes the upper black blob representing the  $\gamma^*$ -parton interaction in Figs. 28 and 29. They combine into an IR finite but collinearly divergent cross section,

$$\sigma_{real+virtual} \simeq \frac{\alpha_s C_F}{\pi} \int_0^{Q^2} \frac{dk_{\perp}^2}{k_{\perp}^2} \int_0^1 \frac{dz}{1-z} [\sigma_h(xzP) - \sigma_h(xP)], \quad (112)$$

where the soft divergence at  $z = 1$  cancels and this cancellation appears as the so-called ‘+’ prescription,

$$\int_0^1 \frac{dz}{(1-z)_+} f(z) \equiv \int_0^1 \frac{dz}{1-z} [f(z) - f(1)]. \quad (113)$$

The collinear divergence in (112) is regulated through a momentum cut-off, called factorisation scale  $\mu_F$ , and absorbed into the definition of the parton densities:

$$\sigma_{real+virtual} \simeq \frac{\alpha_s C_F}{\pi} \int_{\mu_F^2}^{Q^2} \frac{dk_{\perp}^2}{k_{\perp}^2} \int \frac{dx dz}{1-z} [\sigma_h(xzP) - \sigma_h(xP)] q(x, \mu_F^2). \quad (114)$$

This cut-off is arbitrary, so the final physical results must be independent of its value. This gives rise to the DGLAP evolution of the quark densities, which can be seen as the evolution due to radiation between some scale  $\mu_F^2$  below the real and virtual emission in Figs. 28 and 29 and some infinitesimal increase  $(1 + \varepsilon)\mu_F^2$  above.

The result reads

$$\frac{dq(x, \mu_F^2)}{d \ln \mu_F^2} = \int_x^1 \frac{dz}{z} P_{q \leftarrow q}(z) q(x/z, \mu_F^2), \quad P_{q \leftarrow q}(z) = \left( \frac{1+z^2}{1-z} \right)_+. \quad (115)$$

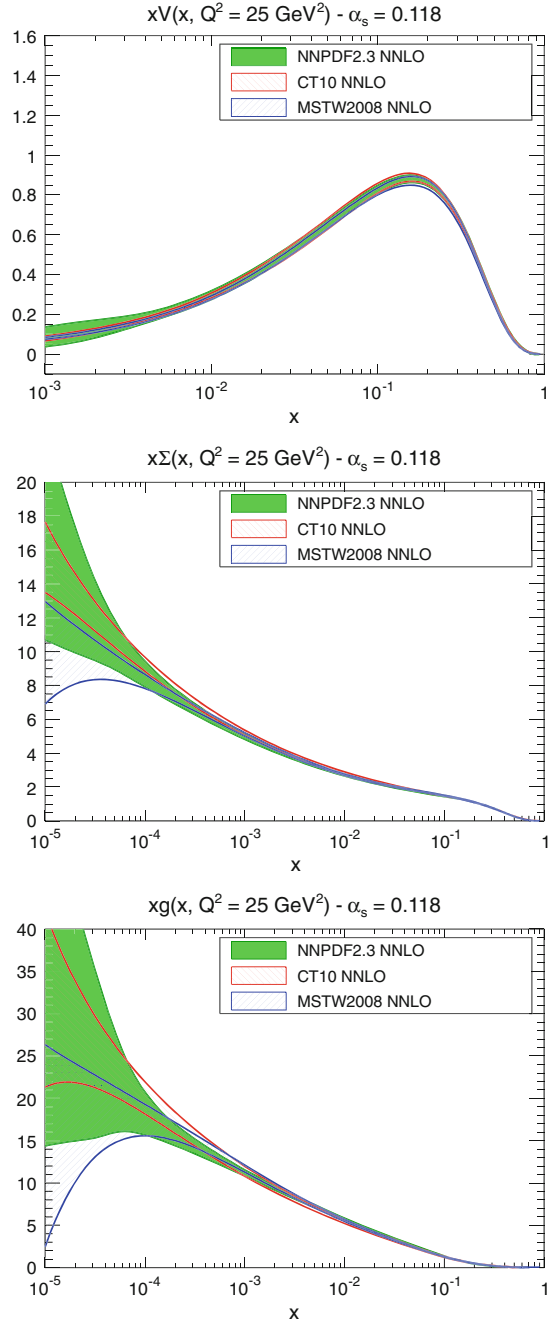
The DGLAP evolution equations are the tools used nowadays to extract the parton densities in proton and nuclei. These quantities are non-perturbative, but their evolution with the factorisation scale, which in DIS is naturally identified with the photon virtuality  $Q^2$ , is controlled by the equations. So the following iterative procedure is used:

1. The parton densities are parametrised at some given low scale  $Q_0$  using some functional form that depends on a series of parameters. Different groups use different functional forms, number of parameters and assumptions in order to reduce the number of parameters, besides momentum and baryon number sum rules. The scale  $Q_0$  has to be low compared with the available range of scales in the experimental data, but larger than  $\Lambda_{QCD}$  in order to apply perturbation theory. A given initial choice of parameters is done.
2. DGLAP evolution is applied to these parton densities.
3. Using the parton densities, now available at all required scales, all cross sections are computed that are believed to be describable in perturbative QCD and for which experimental data exist.
4. Some comparison to experimental data is done, using some criterium as  $\chi^2$ , likelihood, ...
5. If such criterium is found to be optimal e.g. a minimum of the  $\chi^2$ , then the set of parameters is considered to give the best fit and standard error analysis is used to compute the uncertainties in the extracted parton densities. If no, we go back to 1., varying the initial parameters and the procedure is repeated.

Several groups perform this technique. In Fig. 30, some comparison of the results is shown, taken from [44]. The results show an impressive agreement to data, as shown in Fig. 31, providing one of the most stringent tests of perturbative QCD and an analysis of the proton that shows no evidence of substructure down to lengths of order  $10^{-4}$  fm. For the nuclear case, the same procedure is applied, producing similar results that show clearly that the partons densities inside nuclei cannot be considered as the mere superposition of those in protons and neutrons, see Fig. 32. The only limitation in the nuclear case comes from the scarce data, see e.g. [45].

While this procedure is evidently successful, one comment is in order: in the DGLAP evolution equations the variation of the parton densities is proportional to the parton densities themselves, leading to a strong growth of them towards small  $x$ . Such growth strongly suggest that, at some very small  $x$ , non-linear phenomena should appear. In fact, there is strong theoretical evidence that it must be so, see e.g. [47, 48] and references therein. There exist realisations of QCD in which these non-linear phenomena are describable in the weak coupling regime and thus by perturbative techniques. Actually, presently available DIS data can be described in

**Fig. 30** Comparison of different parton densities for valence quarks (*top*), sea quarks (*middle*) and gluons (*bottom*), extracted using DGLAP analyses. (Taken from [44])



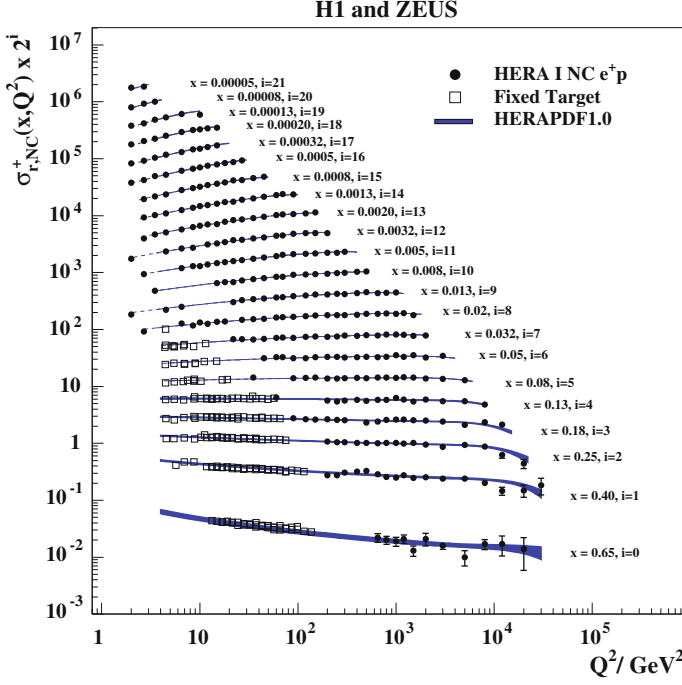


**Fig. 31** Comparison of the results of a DGLAP analysis to DIS experimental data. (Taken from [46])

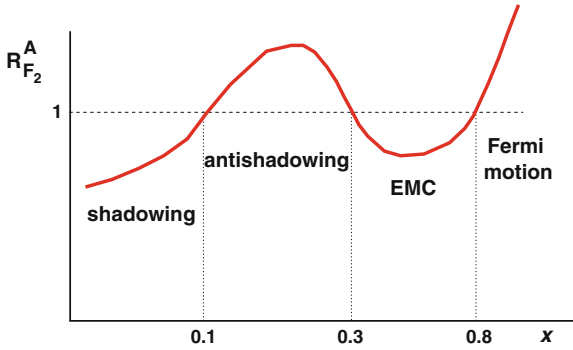


**Fig. 32** Schematic plot showing the different regions in the ratio of structure functions and parton densities in nuclei over those in a nucleon. (Taken from [45])

fixed-order perturbation theory (DGLAP evolution), in schemes that resume not only collinear logarithms like DGLAP does but also soft logarithms present in the splitting kernels, see (100), and non-linear approaches. The present experimental debate lies on where in the kinematic  $x - Q^2$  plane the existence of effects beyond fixed-order

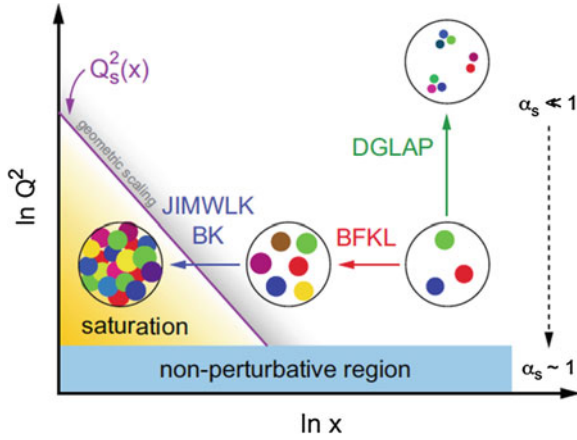


**Fig. 33** Schematic plot of hadron structure showing the linear and non-linear (saturation) regions. (Taken from [47])

perturbation theory becomes mandatory. Figure 33 shows a sketch of the hadron structure in this respect.

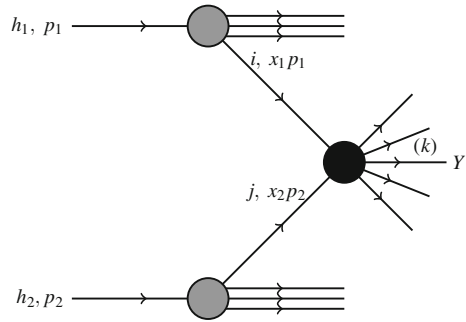
### 8.3 QCD in Hadronic Collisions: Factorisation

Factorisation is the key tool that allows to perform calculations for physical observables in perturbative QCD. It is illustrated in Fig. 34 for hadronic collisions. Mathematically, the cross section in a hadronic collision to produce observable  $Y$  is given by

$$\sigma(h_1(p_1) + h_2(p_2) \rightarrow Y) = \int dx_1 \int dx_2 \sum_{i,j} f_i(x_1) f_j(x_2) \hat{\sigma}(i + j \rightarrow Y) + \mathcal{O}\left(\frac{1}{S^n}\right), \quad (116)$$

where  $f_{i(j)}(x_{1(2)})$  (grey blobs in Fig. 34) is the distribution of parton  $i(j)$  to take momentum fraction  $x_{1(2)}$  from hadron  $h_{1(2)}$ ,  $\hat{\sigma}(i + j \rightarrow Y)$  (black blob in Fig. 34) is the cross section to produce observable  $Y$  from partons  $i$  and  $j$ , and observable  $Y$  may come directly from  $\hat{\sigma}$  (e.g. being a Higgs or electro-weak boson, a photon, . . .), or through a parton  $k$  (then containing a jet reconstruction algorithm, a fragmentation function for the projection of the parton onto a hadron, . . .); PDFs  $f$  (and fragmentation functions) contain a factorisation scale, and  $\hat{\sigma}(i + j \rightarrow Y)$  a renormalisation scale and is computable in perturbation theory; and the corrections are power-suppressed in terms of a given scale  $S$  that is related with the observable, being its mass, energy, transverse momentum, . . .

**Fig. 34** Illustration of factorisation in hadronic collisions



When the scale  $S$  is close to the total available energy in the centre-of-mass, this kind of factorisation is called collinear, and the evolution of PDFs and fragmentation functions is given by the DGLAP equations. The origin of collinear factorisation lies in the separation of scales between the large scale  $S$  of the event and the soft scale  $\Lambda_{QCD}$ , that allows a division between short distance pieces (the hard scattering cross section  $\hat{\sigma}$  computable order by order in perturbation theory and available at next-to-leading order for all observables of interest, and in many cases at next-to-next-to-leading order), and long distance ones (the PDFs and fragmentation functions). This factorisation has been proved, for inclusive enough observables like 1-particle or 2-jet production and for specific kinematic configurations, in  $e^+e^-$  annihilation, in DIS and for the Drell-Yan process. It is assumed to work in hadron-hadron collisions.

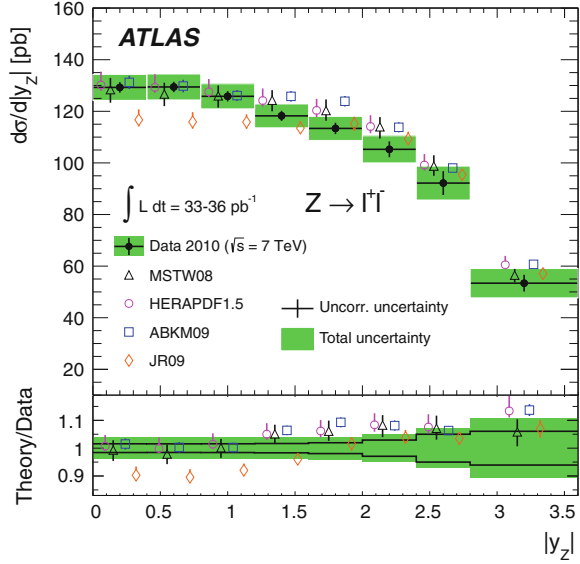
It should be noted that large logarithms may appear for given kinematic configurations that need to be resummed, and that other kinds of factorisation exist like  $k_T$ -factorisation for  $E_{cm} \gg S \gg \Lambda_{QCD}$ .

In Fig. 35 we show one comparison of perturbative calculations with hadron-hadron data at the LHC. It can be seen that the experimental results are sensitive to the differences among the different PDF sets. In fact, this is the main source of uncertainty in the extrapolations for precision measurements and searches for beyond-the-Standard-Model physics in the proposed high-luminosity phase of the LHC [49].

## 8.4 QCD Radiation

Radiation determines most of the features in perturbative QCD. Let us start by a single emitter, as pictured in Fig. 23. Obviously, an isolated on-shell massless particle cannot radiate. Some virtuality, of order  $k_\perp^2/[x(1-x)]$ , has to be allowed for radiation to occur. The process of multiple gluon emission proceeds through the iteration of emission given in the soft and collinear limits by the probability in (100). This iteration gives rise to large logarithms in the limit in which subsequent emissions  $i = 1, 2, 3, \dots$  are strongly ordered in both longitudinal and transverse momentum i.e.

**Fig. 35** Rapidity distribution of  $Z^0$  bosons decaying into  $l^+l^-$  measured by the ATLAS Collaboration at the LHC, compared to next-to-next-to-leading order results using different PDFs. (Taken from [50])



$$x_1 \gg x_2 \gg \cdots \gg x_n, \quad k_{\perp,1} \ll k_{\perp,2} \ll \cdots \ll k_{\perp,n} \quad (117)$$

(for initial state radiation; for final state radiation, the ordering in  $k_{\perp}$  is the opposite, from a high to a low virtuality). These orderings gives rise to powers of two types of logarithms, of  $x$  and of  $k_{\perp}$ , and this limit is known as the double-leading-logarithmic limit.

On the other hand, a single massive particle cannot emit collinearly, a phenomenon known as dead cone effect, exemplified in Fig. 36.

Now we consider two emitters: two highly energetic quark and antiquark originated at some given position and with angular separation  $\theta_{p\bar{p}}$ . In the limit of soft

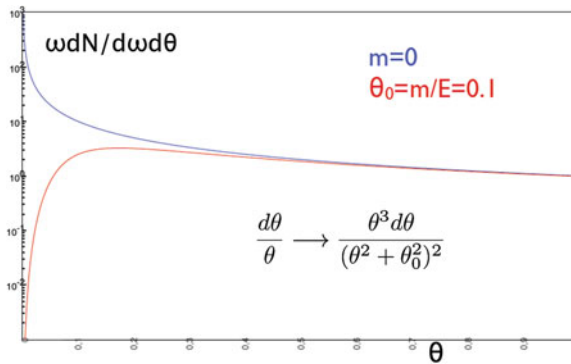
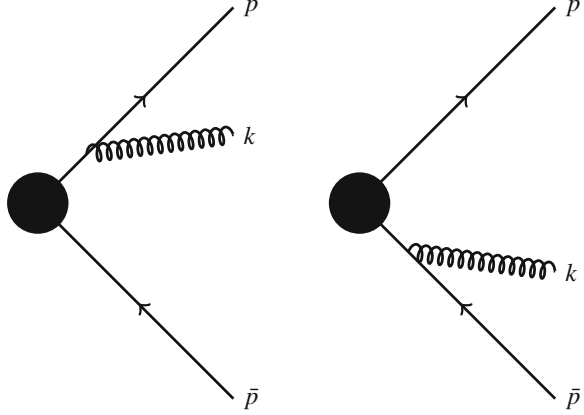


**Fig. 36** Illustration of the difference of the gluon radiation spectrum off massless and massive quarks versus the emission angle for fixed gluon energy, in arbitrary units



**Fig. 37** Diagrams contributing to gluon emission off a  $q\bar{q}$  antenna in the soft limit



emitted gluons, the diagrams that contribute to gluon radiation at the lowest order are given in Fig. 37. The gluon radiation spectrum is given by

$$(2\pi)^2 E \frac{dN}{d^3k} = \alpha_s C_F \frac{p \cdot \bar{p}}{(p \cdot k)(\bar{p} \cdot k)}. \quad (118)$$

It turns out that the spectrum can be separated in parts that contain collinear divergences either from the quark or from the antiquark,  $dN = dN_q + dN_{\bar{q}}$ . After azimuthal average, the gluon spectrum off the quark (or antiquark) takes the form

$$dN_q \propto \alpha_s \frac{d\omega}{\omega} \frac{d\theta_{pk}}{\theta_{pk}} \Theta(\theta_{p\bar{p}} - \theta_{pk}), \quad (119)$$

where  $\Theta$  is the step function. In this way, quantum interferences provide a probabilistic picture of gluon emission, and this gluon emission features angular ordering: gluon emission at angles larger than the opening angle of the  $q\bar{q}$  pair are suppressed. The intuitive explanation of this phenomenon is as follows (we use small angle approximations): The decoherence time of the emitted gluon (i.e. the time it takes to decohere the gluon from the  $q\bar{q}$  pair) is  $t_c \sim \omega/k_\perp^2$ . The transverse resolution of the gluon is  $D_g \sim 1/k_\perp$ . The separation of the  $q\bar{q}$  pair at decoherence time is  $D_{q\bar{q}} = \theta_{p\bar{p}} t_c = \theta_{p\bar{p}}/(k_\perp \theta_{pk})$ . Then the condition that, in order to be radiated, the gluon should resolve the  $q\bar{q}$  pair in order to ‘see’ a non-zero colour charge leads to  $D_{q\bar{q}} > D_g \Rightarrow \theta_{pk} < \theta_{p\bar{p}}$ . While this reasoning is restricted to a colour antenna in the singlet representation, angular ordering holds for arbitrary colour representations: When the antenna is a non-singlet colour state, radiation outside the cone,  $\theta_{pk} > \theta_{p\bar{p}}$ , happens with the strength given by the total colour charge i.e. the pair acts as a single emitter with the charge of the pair—the charge of the parent parton of the  $q\bar{q}$  pair. In this sense, a simple probabilistic picture emerges, which is implemented e.g. in Monte Carlo generators: radiation inside the cone determined by the pair opening angle,  $\theta < \theta_{p\bar{p}}$ , takes place as independent radiation off each of the partons, while

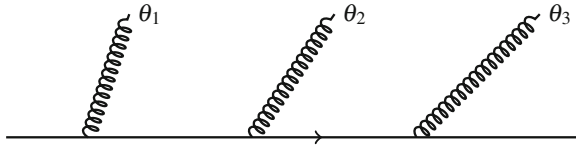


**Fig. 38** Multiple gluon emission off a quark with different emission angles, showing angular ordering between subsequent emissions

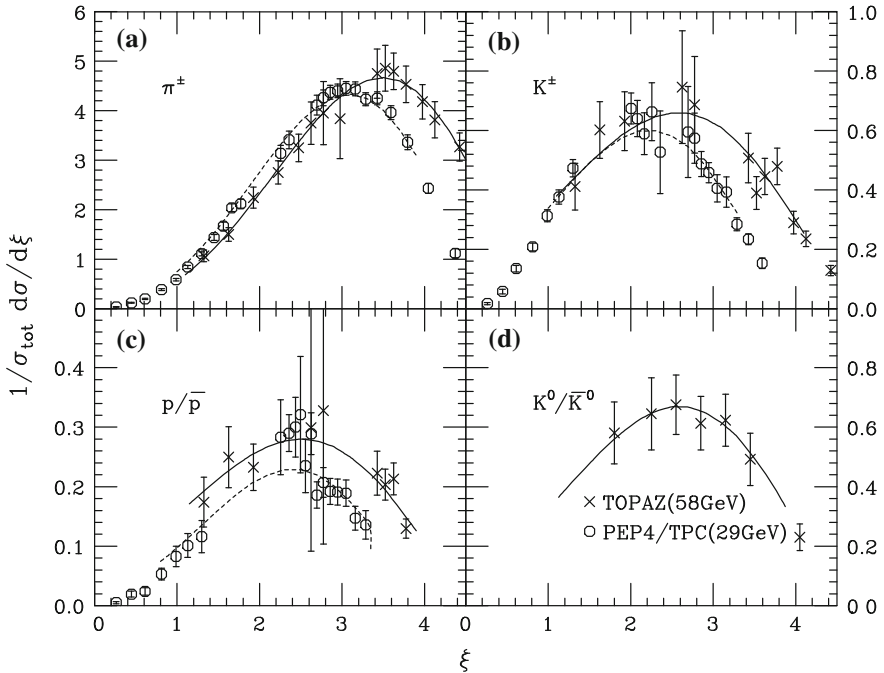


**Fig. 39** Comparison of experimental data on particle distribution in  $\xi \simeq \ln(E_{jet}/E_{hadron})$ . Large  $\xi$  corresponds to soft particle production. (Taken from [52])

radiation outside the cone,  $\theta > \theta_{p\bar{p}}$ , can be reinterpreted as radiation off the parent parton, so that the angular ordering can be effectively introduced.

It should be noted that coherence, through the restriction in the phase space for multiple gluon emission (Fig. 38) that angular ordering provides, implies a strong reduction of particle multiplicities inside jets (particles produced by radiation off a highly energetic parton) in the soft sector compared to successive independent, incoherent emissions. The agreement that angular ordering yields can be seen in Fig. 39. It also provides the basis for a probabilistic interpretation of parton branching that lies at the root of existing implementation of the QCD showering process in Monte Carlo simulators [51], with different ordering variables for the development in the cascade that at high energies are all of them equivalent to emission angle.

It is obvious that, in a Quantum Field Theory like QCD, we would like to compute diagrams with any number of external legs that would give the cross section for production of any number of partons. This is not possible for a large number even at a tree level, and constitutes a subject on its own. But the structure of coherent QCD radiation provides a probabilistic picture that allows a sequential treatment of the branching process: iteration of emission kernel at some given value of the ordering variable  $t_1 \times$  probability of no resolvable emission (called Sudakov form factor) between  $t_1$  and  $t_2 \times$  emission kernel at  $t_2 \times \dots$ , that should give the dominant contribution to multiplicities of produced partons.

## 8.5 Jets

In high-energy collisions, the strong interaction tends to produce collimated showers of hadrons, called jets, see [53] and references therein for full information. This is due to several characteristics of QCD: collinear singularities of the emission probabilities, gluon self-interaction, coherence between emitters and, on a more fundamental level, asymptotic freedom and confinement. In principle, in perturbation theory one would like to be able to work with partons but, even at a perturbative level, partons are ill-defined concepts due to the existence of IR and collinear divergences that make it impossible to distinguish between one parton and two collinear ones, or one hard and one very soft parton.

Therefore, jets require a definition and, in order to make it possible a meaningful comparison between experiment and theory, the definition (the counting of the number of jets in an event and their energy) should be:

1. Stable at all order in perturbation theory under the splitting of a parton into two collinear ones or into one very hard and one very soft.
2. Insensitive to the parton-to-hadron transition, so it should be defined in terms of flows of energy i.e. calorimetric measurements.

The problem can be seen in the fact that the definition should be such that the cancellation of singularities between virtual and real corrections, see Fig. 40, happens in order to render a finite cross section.

Jets are defined in the plane determined by the pseudo rapidity and azimuthal angle. Simplifying, there are two types of algorithms for jet reconstruction. One kind of them uses a seed in order to start clustering particles into jets, thus privileging a particle. This kind of algorithms, with many different variations, are IRC unsafe due to an incomplete cancellation between real and virtual corrections, and present problems for the comparison between theory and experiment. They can be made finite at some given order of perturbation theory, but they fail at the next order or when using resummations. This is illustrated in Figs. 41 and 42.

It turns out that seedless or sequential recombination algorithms are IRC safe. Let us briefly define how they work (in the basic implementation). For a list of particles with  $\eta_i, p_{\perp,i}, \phi_i, i = 1, 2, \dots, N$ , we define

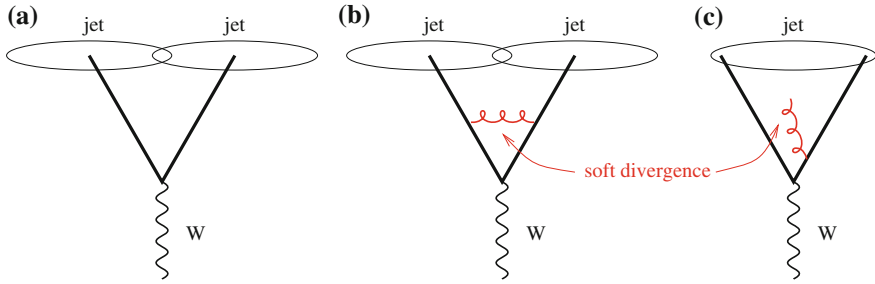


**Fig. 40**  $W$  decaying into two quark jets (a), the virtual (b) and real (c) next-to-leading corrections whose singularities must cancel in order to make a final finite result. (Taken from [53])

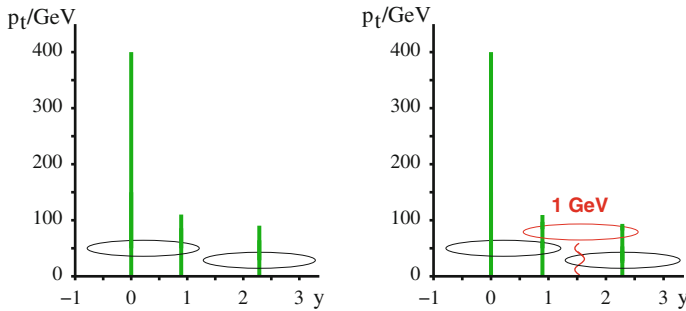


**Fig. 41** Exemplification of how the addition of one soft particle (red wavy line) varies the counting of jets between the plot on the left and the plot on the right, thus showing the problems of algorithms that use a seed. The hardest particle of the event is used as a seed and the value of the parameters inside which particles are merged into jet is smaller than the distance between the first and third particle (from left to right) in the plot on the left. (Taken from [53])

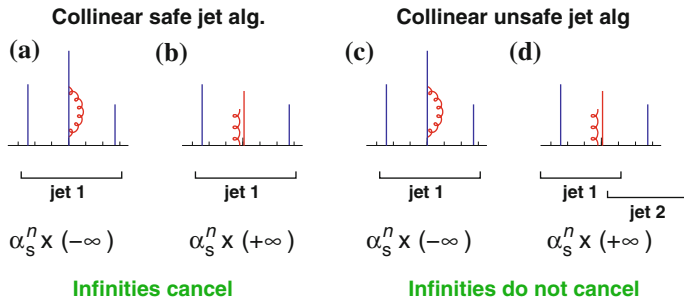


**Fig. 42** Plots on the left example of how the addition of an collinear gluons does not alter the counting of jets for seedless algorithms. Plots on the right example of the contrary in an algorithm that uses a seed, in this case the hardest particle in the event. (Taken from [53])

$$d_{iB} = p_{\perp,i}^{2n}, \quad d_{ij} = \min(p_{\perp,i}^{2n}, p_{\perp,j}^{2n}) \frac{\Delta R_{ij}^2}{R^2}, \quad \Delta R_{ij}^2 = (\eta_i - \eta_j)^2 + (\phi_i - \phi_j)^2. \quad (120)$$

Now we proceed sequentially:

1. Find the minimum of all  $\{d_{iB}, d_{ij}\}$ .
2. If it is a  $d_{iB}$ , remove particle  $i$ , that it is called a jet, from the list.
3. If it is a  $d_{ij}$ , merge  $i$  and  $j$  and redo the list.
4. If the list is not exhausted, go back to 1.

All in all, in this simplest variant any algorithm is defined by the prescription of merging particles (the most widely used nowadays is adding the four-momentum of the particles) and by the value of  $R$ . Different values of  $n$  produce different algorithms:  $n = 1$  gives the so-called  $k_T$  algorithm,  $n = 0$  Cambridge/Aachen, and  $n = -1$  anti- $k_T$ . The latter is the most commonly employed option at the LHC, and gives rise to quite ‘conical’ jets, see Fig. 43 for an illustration. In the past, sequential recombination algorithms were very expensive computationally which prevented their application for hadronic collisions, but new developments have allowed large improvements in computing time, making them practical tools of wide use at the LHC.

One very important aspect is the energy of the parton that is reconstructed when defining a ‘conical’ jet of radius  $R$  (note that while the definition of a jet as a cone in the  $\eta \times \phi$  space is not, in principle, IRC safe, there exist seedless cone algorithms that are IRC safe and that jets defined through the anti- $k_T$  algorithm have a conical shape). The difference between the energy of the jet and that of the parton receives 3 contributions:

$$\langle p_{\perp,jet} - p_{\perp,parton} \rangle = ap_{\perp}\alpha_s \ln R - \frac{b}{R} + cR^2. \quad (121)$$

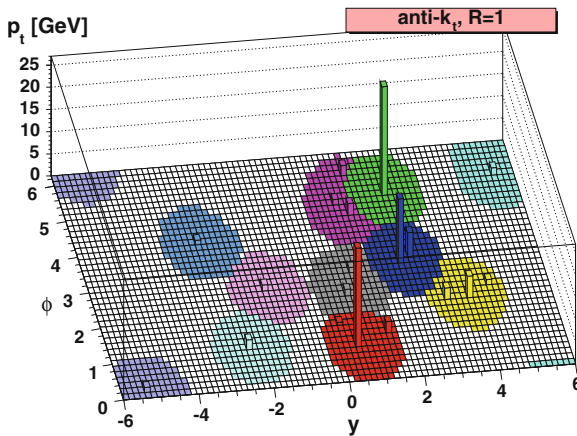


**Fig. 43** Illustration of the jets in a pp event and their shapes in the  $\eta \times \phi$  plane, defined using the anti- $k_T$  algorithm with  $R = 1$ . (Taken from [53])

The three contributions to the r.h.s. of this equation are interpreted as follows:

- The first contribution has a radiative origin and corresponds to the energy ( $p_{\perp}$ ) of the parton that is sent outside the cone by QCD radiation. Thus the presence of the logarithm and of the coupling constant. The constant  $a$  is computable using perturbative techniques.
- The second contribution has a non-perturbative origin and accounts for energy of the parton that is sent outside the cone by hadronisation effects. It is usually estimated using Monte Carlo models that consider hadronisation of partons into hadrons.
- The third contribution accounts for the background—the contribution from particles in the collisions that do not come from the parton that originates the jet—that may have three origins: additional soft or hard parton-parton interactions in the collision to the one that originates the parton that produces the jet (the so-called underlying event); additional nucleon-nucleon collisions in the case of nuclear projectiles and targets (called underlying event or heavy-ion background, although it does not require a truly heavy ion); and additional projectile-target collisions that come from the fact that such possibility exists when bunches of particles cross in the interaction regions of the accelerator (so-called pile-up, that maybe as high as 100 in pp collisions at the LHC). Although a strict distinction between particles in the jet and in the background is senseless from both a practical and a theoretical point of view, techniques have been developed to deal with this problem that may be crucial for extracting information off jet measurements. Note that in a head-on PbPb collision at the LHC, the background contribution may be as high as  $\mathcal{O}(100 \text{ GeV})$  per unit area in the  $\eta \times \phi$  plane.

Jet measurements provide one of the most impressive checks of perturbative QCD, see the agreement between experimental data and theoretical calculations at next-to-leading order in Fig. 44 that extends through several orders of magnitude in the measured cross sections.

Finally, note that jets are not only very interesting objects in QCD, but also most required tools in other topics as Standard Model or Beyond the Standard Model studies. For example, jet reconstruction is required for determining the couplings of the Higgs boson to quarks, couplings that may not only verify their expected dependency with the quark mass in the Standard Model but also be sensitive to new physics. Jets are also required to reconstruct hadronic decays of electro-weak bosons.

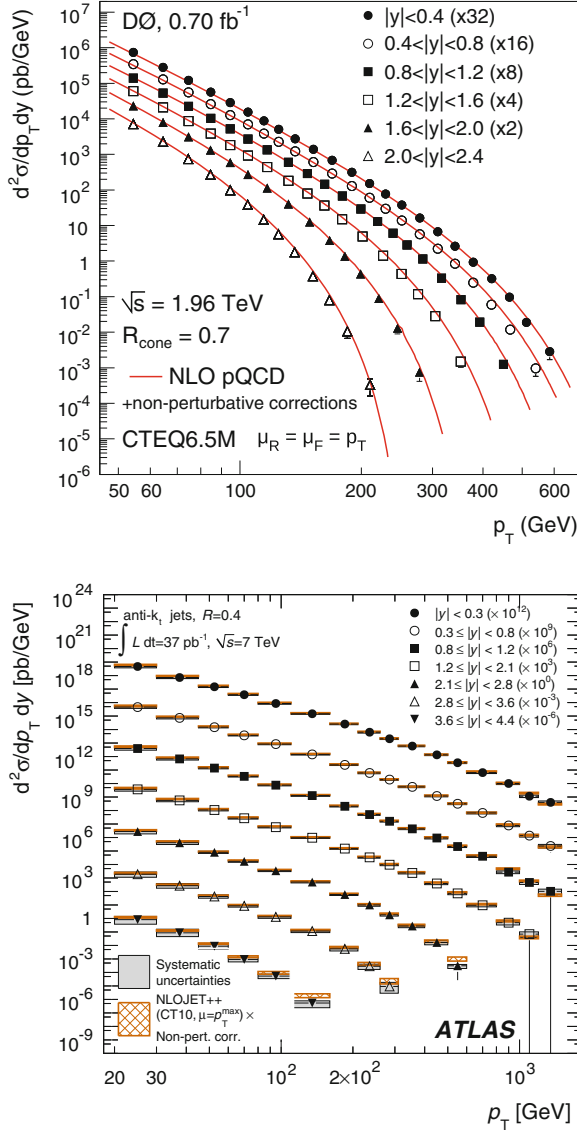


**Fig. 44** Comparison of experimental data on single-inclusive jet cross sections at different pseudo-rapidities to perturbative QCD calculations at next-to-leading order. *Top* data from the DO Collaboration at the Tevatron (taken from [54].) *Bottom* data from the ATLAS Collaboration at the LHC (taken from [55])

**Acknowledgments** We thank Tolga Altinoluk for help in producing Feynman diagrams. This work is supported by the European Research Council grant HotLHC ERC-2011-StG-279579; by Ministerio de Ciencia e Innovación of Spain under projects FPA2009-11951 and FPA2011-22776; by Xunta de Galicia (Consellería de Educación and Consellería de Innovación e Industria—Programa Incite); by the Spanish Consolider-Ingenio 2010 Programme CPAN and by FEDER.

## References

1. D.J. Gross, F. Wilczek, Phys. Rev. Lett. **30**, 1343–1346 (1973)
2. H.D. Politzer, Phys. Rev. Lett. **30**, 1346–1349 (1973)
3. F.J. Yndurain, *The Theory of Quark and Gluon Interactions* (Springer, Berlin, 1999)
4. P. Pascual, R. Tarrach, *QCD: Renormalization for the Practitioner* (Springer, New York, 1984)
5. A.V. Smilga, *Lectures on Quantum Chromodynamics* (World Scientific, London, 2001)
6. B.L. Ioffe, V.S. Fadin, L.N. Lipatov, *Quantum Chromodynamics: Perturbative and Nonperturbative Aspects* (Cambridge University Press, Cambridge, 2010)
7. R.K. Ellis, W.J. Stirling, B.R. Webber, *QCD and Collider Physics* (Cambridge University Press, Cambridge, 2003)
8. E. Leader, E. Predazzi, *An Introduction to Gauge Theories and Modern Particle Physics*, vols. 1 and 2 (Cambridge University Press, Cambridge, 1996)
9. Y.L. Dokshitzer, V.A. Khoze, A.H. Mueller, S.I. Troyan, *Basics of Perturbative QCD* (Editions Frontières, Gif-sur-Yvette, 1991)
10. H. Fritzsch, M. Gell-Mann, H. Leutwyler, Phys. Lett. **B47**, 365–368 (1973)
11. S. Bethke, Eur. Phys. J. **C64**, 689–703 (2009)
12. R. Alkofer, J. Greensite, J. Phys. G **34**, S3 (2007). [arXiv:hep-ph/0610365](https://arxiv.org/abs/hep-ph/0610365)
13. J. Greensite, Lect. Notes Phys. **821**, 1 (2011)
14. Z. Fodor, C. Hoelbling, Rev. Mod. Phys. **84**, 449 (2012). [arXiv:1203.4789](https://arxiv.org/abs/1203.4789) [hep-lat]
15. G.F. Sterman, S. Weinberg, Phys. Rev. Lett. **39**, 1436 (1977)
16. A. Dobado, A. Gomez-Nicola, A.L. Maroto, J.R. Pelaez, *Effective Lagrangians for the Standard Model* (Springer, Berlin, 1997)
17. Y. Nambu, Phys. Rev. Lett. **4**, 380 (1960)
18. J. Goldstone, Nuovo Cimento **19**, 154 (1961)
19. H.-Y. Cheng, Phys. Rep. **158**, 1 (1988)
20. R.D. Peccei, H.R. Quinn, Phys. Rev. D **16**, 1791 (1977)
21. G. 't Hooft, Phys. Rev. Lett. **37**, 8 (1976)
22. G. 't Hooft, Phys. Rep. **142**, 357 (1986)
23. T.D. Lee, G.C. Wick, Phys. Rev. D **9**, 2291 (1974)
24. J.C. Collins, M.J. Perry, Phys. Rev. Lett. **34**, 1353 (1975)
25. J. Hofmann, H. Stöcker, W. Scheid, W. Greiner, in *Report of the Workshop on BeV/Nucleon Collisions of Heavy Ions: How and Why, Bear Mountain*, New York, 29 Nov–1 Dec 1974
26. B.A. Freedman, L.D. McLerran, Phys. Rev. D **16**, 1169 (1977)
27. N. Cabibbo, G. Parisi, Phys. Lett. B **59**, 67 (1975)
28. E.V. Shuryak, Phys. Lett. B **78**, 150 (1978)
29. E.V. Shuryak, Sov. J. Nucl. Phys. **28**, 408 (1978)
30. H. Satz, Lect. Notes Phys. **841**, 1 (2012)
31. F. Karsch, Lect. Notes Phys. **583**, 209 (2002) [arXiv:0711.0656](https://arxiv.org/abs/hep-lat/0711.0656) [hep-lat]
32. F. Karsch, J. Phys. Conf. Ser. **46**, 122 (2006) [arXiv:0711.0661](https://arxiv.org/abs/hep-lat/0711.0661) [hep-lat]
33. J.D. Bjorken, Phys. Rev. D **27**, 140 (1983)
34. C.-Y. Wong, *Introduction to High-energy Heavy-ion Collisions* (World Scientific, Singapore, 1994)
35. R. Hwa (ed.), *Quark-Gluon Plasma*, vol. 1 (World Scientific, Singapore, 1990)
36. R. Hwa (ed.), *Quark-Gluon Plasma*, vol. 2 (World Scientific, Singapore, 1995)



37. R. Hwa, X.N. Wang (eds.), *Quark-Gluon Plasma*, vol. 3 (World Scientific, Singapore, 2004)
38. R. Hwa, X.N. Wang (eds.), *Quark-Gluon Plasma*, vol. 4 (World Scientific, Singapore, 2010)
39. C. Pajares, Yu.M. Shabelski, *Relativistic Nuclear Interactions* (URSS, Moscow, 2007)
40. J.-P. Blaizot, Lect. Notes Phys. **583**, 117 (2002). [arXiv:hep-ph/0107131](#)
41. G.P. Salam, CERN Yellow Report CERN-2010-002, 45–100. [arXiv:011.5131](#) [hep-ph]
42. V.V. Ezhela, S.B. Lugovsky, O.V. Zenin, [arXiv:hep-ph/0312114](#)
43. J. Beringer et al., [Particle Data Group Collaboration], Phys. Rev. D **86**, 010001 (2012)
44. R.D. Ball, S. Carrazza, L. Del Debbio, S. Forte, J. Gao, N. Hartland, J. Huston, P. Nadolsky et al., JHEP **1304**, 125 (2013). [arXiv:1211.5142](#) [hep-ph]
45. N. Armesto, J. Phys. G **32**, R367 (2006). [arXiv:hep-ph/0604108](#)
46. F.D. Aaron et al. [H1 and ZEUS Collaboration], JHEP **1001**, 109 (2010). [arXiv:0911.0884](#) [hep-ex]
47. A. Accardi, J.L. Albacete, M. Anselmino, N. Armesto, E.C. Aschenauer, A. Bacchetta, D. Boer, W. Brooks et al., [arXiv:1212.1701](#) [nucl-ex]
48. Yu.V. Kovchegov, E.M. Levin, *Quantum Chromodynamics at High Energy* (Cambridge University Press, Cambridge, 2012)
49. ATLAS Collaboration, ATL-PHYS-PUB-2012-004
50. G. Aad et al., [ATLAS Collaboration], Phys. Rev. D **85**, 072004 (2012). [arXiv:1109.5141](#) [hep-ex]
51. A. Buckley, J. Butterworth, S. Gieseke, D. Grellscheid, S. Hoche, H. Hoeth, F. Krauss, L. Lonnblad et al., Phys. Rep. **504**, 145 (2011). [arXiv:1101.2599](#) [hep-ph]
52. R. Itoh et al., [TOPAZ Collaboration], Phys. Lett. B **345**, 335 (1995). [arXiv:hep-ex/9412015](#)
53. G.P. Salam, Eur. Phys. J. C **67**, 637 (2010). [arXiv:0906.1833](#) [hep-ph]
54. V.M. Abazov et al., [D0 Collaboration], Phys. Rev. D **85**, 052006 (2012). [arXiv:1110.3771](#) [hep-ex]
55. G. Aad et al., [ATLAS Collaboration], Phys. Rev. D **86**, 014022 (2012). [arXiv:1112.6297](#) [hep-ex]

Lectures on Particle Physics, Astrophysics and  
Cosmology

Proceedings of the Third IDPASC School, Santiago de  
Compostela, Spain, January 21 -- February 2, 2013  
Merino, C. (Ed.)

2015, XXI, 480 p. 246 illus., 151 illus. in color.,  
Hardcover

ISBN: 978-3-319-12237-3